# Subseasonal Meteorological Drought Development over the Central United States during Spring

BOR-TING JONG,[a,b,c] MATTHEW NEWMAN,[a,d] AND ANDREW HOELL[a]

[a] *NOAA Physical Sciences Laboratory, Boulder, Colorado*
[b] *NOAA Geophysical Fluid Dynamics Laboratory, Princeton, New Jersey*
[c] *Program in Atmospheric and Oceanic Sciences, Princeton University, Princeton, New Jersey*
[d] *Cooperative Institute for Research in Environmental Sciences, University of Colorado Boulder, Boulder, Colorado*

(Manuscript received 7 June 2021, in final form 3 November 2021)

ABSTRACT: Diagnosis of rapidly developing springtime droughts in the central United States has mostly been made via numerous individual case studies rather than in an aggregate sense. This study investigates common aspects of subseasonal "meteorological drought" evolution, here defined as persistent precipitation minus evapotranspiration ($P - ET$) deficits, revealed in early (1 April–15 May) and late (16 May–30 June) spring composites of 5-day running mean JRA-55 reanalysis data for three different central U.S. regions during 1958–2018. On average, these droughts are initiated by a quasi-stationary Rossby wave packet (RWP), propagating from the western North Pacific, which arises about a week prior to drought onset. The RWP is related to a persistent ridge west of the incipient drought region and strong subsidence over it. This subsidence is associated with low-level divergent flow that dries the atmosphere and suppresses precipitation for roughly 1–2 weeks, and generally has a greater impact on the local moisture budget than does reduced poleward moisture transport. The resulting "dynamically driven" evaporative demand corresponds to a rapid drying of the root-zone soil moisture, which decreases around 40 percentiles within about 10 days. Anomalous near-surface warmth develops only after the $P - ET$ deficit onset, as does anomalously low soil moisture that then lingers a month or more, especially in late spring. The horizontal scale of the RWPs, and of the related drought anomalies, decreases from early to late spring, consistent with the climatological change in the Pacific Rossby waveguide. Finally, while this composite analysis is based upon strong, persistent $P - ET$ deficits, it still appears to capture much of the springtime development of "flash droughts" as well.

KEYWORDS: Drought; Subseasonal variability; Spring season; Hydrologic cycle; North America

## 1. Introduction

Drought is induced by a persistent deficit in surface water availability, driven by a decrease in the moisture source (deficit of precipitation) and/or an increase in the moisture sink (enhanced evapotranspiration). Extreme atmospheric anomalies persisting for only a few weeks can trigger swift drought development on subseasonal time scales (Lyon and Dole 1995; Mo and Lettenmaier 2015; Koster et al. 2019), a phenomenon sometimes called flash drought (e.g., Otkin et al. 2013, 2018; Pendergrass et al. 2020). Rapidly intensifying droughts can be hazardous to agriculture, particularly during springtime in the central United States when both rainfall (e.g., Englehart and Douglas 2003; Mo 2011) and crop development (e.g., Hu and Buyanovsky 2003; Hansen et al. 2012; Huang et al. 2015; Anderson et al. 2017) are at their peak.

A quintessential flash drought, the 2012 Great Plains drought, began in May 2012 with a persistent precipitation deficit and warm temperature anomalies associated with a steep decline in soil moisture over the central United States (e.g., Otkin et al. 2016). The resulting soil moisture deficit, which continued to increase with additional persistent precipitation deficit events from June through early July (Hoerling et al. 2014; DeAngelis et al. 2020), was exacerbated by land–atmosphere coupling (e.g., Basara et al. 2019; DeAngelis et al. 2020). According to the U.S. Drought Monitor (Svoboda et al. 2002), drought severity in the central United States intensified by up to four categories from May to August (Otkin et al. 2018; Pendergrass et al. 2020). While many mechanisms contributed to this drought's evolution, the persistent precipitation deficit and warm temperature anomalies in the spring were likely critical components.

Several other springtime droughts have had characteristics similar to those of the 2012 drought. Each has been the focus of case studies aimed at capturing key details of each drought's evolution along with its most relevant physical processes. The most intensively studied droughts, listed in Table 1, are only a subsample of all springtime subseasonal droughts over the last several decades. Other droughts that received relatively less attention are noted, including the 1963 drought over the central United States (Diaz 1983), the 1998 Oklahoma–Texas drought (e.g., Hong and Kalnay 2000), the 2006 Great Plains drought (e.g., Dong et al. 2011; DeAngelis et al. 2020), and the 2007 drought over the Ohio Valley (e.g., Otkin et al. 2013).

However, there have been far fewer attempts at condensing various salient details of these case studies into a comprehensive picture of how subseasonal springtime U.S. droughts evolve. Some studies have focused on local drought characteristics (e.g., Diaz 1983; Englehart and Douglas 2003), while

Supplemental information related to this paper is available at the Journals Online website: https://doi.org/10.1175/JCLI-D-21-0435.s1.

*Corresponding author*: Bor-Ting Jong, bor-ting.jong@noaa.gov

DOI: 10.1175/JCLI-D-21-0435.1

TABLE 1. Previous studies on the five most notable springtime subseasonal drought developments in 1958–2018, including the main drought area and the drought evolutions.

| Event | Region | Onset and evolution | Topics | References |
|---|---|---|---|---|
| 1980 | Great Plains, extending to the eastern United States | Anomalous large-scale circulations developed rapidly, within a week period, near the end of May, imposing a persistent anomalous ridge over the southern Plains and leading to the extensive drought condition from June to September. | Evolutions of regional meteorological conditions | Karl and Quayle (1981), Mo and Lettenmaier (2016) |
| | | | Remote SST forcing and teleconnections | Namias (1982) |
| | | | Associated large-scale atmospheric circulations | Mo and Lettenmaier (2016) |
| | | | Remote SST forcing and teleconnections triggered the drought onset in the late spring; land–atmosphere feedback prolonged the drought condition through the summer | Namias (1983), Lyon and Dole (1995) |
| | | | Relative roles of SST forcing vs soil moisture forcing | Wolfson et al. (1987) |
| 1988 | Across the contiguous United States | Persistent precipitation deficit began in March but rapidly exacerbated from late May and extended through summer, caused by two rapidly developing large-scale wave trains across the North Pacific, imposing anomalous ridges over the Great Plains near the end of May and mid- to late June. | Remote SST forcing and teleconnections | Palmer and Branković (1989), Trenberth et al. (1988), Mo et al. (1991), Chen and Newman (1998) |
| | | | Role of internal atmospheric variability | Seager and Hoerling (2014) |
| | | | Role of large-scale Rossby wave-trains | Wang et al. (2017) |
| | | | Relative roles of remote diabatic heating and transient eddies fluxes | Liu et al. (1998) |
| | | | Remote SST forcing and teleconnections drove drought development in the late spring; land–atmosphere feedback prolonged the drought condition through the summer | Namias (1991), Lyon and Dole (1995), Trenberth and Branstator (1992), Trenberth and Guillemot (1996) |
| | | | Relative roles of SST forcing vs local land–atmosphere feedback | Atlas et al. (1993) |
| | | | Predictability and model predictive skill | Namias (1991) |
| 2011 | Mostly entire Texas, but also extended to Oklahoma and Kansas | Persistent precipitation deficit began in the winter of November 2010. Suppressed convection in April 2011 intensified the drought condition rapidly and led to extreme dry and record-breaking heat in the following summer. | Evolutions of regional drought indices | Otkin et al. (2013) |
| | | | Local thermodynamics structure and land–atmosphere feedback | Fernando et al. (2016) |
| | | | Regional moisture transport and recycling | Erfanian and Fu (2019), Roy et al. (2019) |
| | | | Remote SST forcing and teleconnections | Hoerling et al. (2013), Seager et al. (2014), Wang et al. (2014), Fernando et al. (2016) |
| | | | Potential role of human-induced climate change | Hoerling et al. (2013) |
| | | | Predictability and model predictive skill | Seager et al. (2014) |
| 2012 | Extensive central United States | Persistent precipitation deficit and warm anomalies in mid-May induced rapid decline in soil moisture and the onset of the drought. Another stronger and persistent precipitation deficit and heat wave in late June | Evolutions of local land conditions | Otkin et al. (2016, 2018), Basara et al. (2019), DeAngelis et al. (2020) |
| | | | Regional moisture transport and recycling | Basara et al. (2019), Erfanian and Fu |

TABLE 1. (*Continued*)

| Event | Region | Onset and evolution | Topics | References |
|---|---|---|---|---|
| | | through early July accelerated the drought development. | | (2019), Roy et al. (2019) |
| | | | Role of SST forcing vs internal atmospheric variability | Kumar et al. (2013), Hoerling et al. (2014) |
| | | | Remote SST forcing and teleconnections | Wang et al. (2014) |
| | | | Predictability and model predictive skill | AghaKouchak (2014), Kam et al. (2014), PaiMazumder and Done (2016), DeAngelis et al. (2020) |
| 2017 | The northern Great Plains, including the Dakotas and Montana | Persistent precipitation deficit began in April and extended into August. Soil moisture swiftly declined in late May, from above normal to drought condition (20th percentile) within few weeks. | Evolutions of regional meteorological conditions | Gerken et al. (2018), Hoell et al. (2019b, 2020), Chen et al. (2020), Pendergrass et al. (2020) |
| | | | Remote SST forcing and large-scale circulations | Wang et al. (2019) |
| | | | Contribution of human-induced climate change | Hoell et al. (2019a,b), Wang et al. (2019) |
| | | | Forecasting skill of the potential flash drought development tool used in NOAA Climate Prediction Center (CPC) Monthly Drought Outlook | Chen et al. (2020) |
| | | | Predictability and model predictive skill | Hoell et al. (2019b) |

studies that also included large-scale atmospheric circulation anomalies mostly focused on summer (e.g., Chang and Wallace 1987; Schiraldi and Roundy 2017). Otherwise, systematic diagnoses of the evolution of persistent atmospheric conditions and their resultant impacts on drought development have considered seasonal or longer time scales (e.g., Mo 2011; Livneh and Hoerling 2016; Schubert et al. 2016; Seager et al. 2019).

This study aims to develop a more comprehensive picture of the atmosphere's role in initiating rapid development of subseasonal droughts during springtime (April–June) in the central United States. We base our analysis upon atmospheric moisture deficits rather than soil moisture deficits; that is, we consider what is sometimes called "meteorological drought" rather than "soil moisture drought" or "agricultural drought" (e.g., Wilhite and Glantz 1985; Van Loon et al. 2016; Hao et al. 2018). Meteorological drought represents a period of anomalously dry weather patterns dominating a region (e.g., Van Loon et al. 2016; NIDIS 2021), and has usually been solely defined based upon a persistent precipitation deficit (e.g., Englehart and Douglas 2003; Koster et al. 2009; Mo 2011; Quan et al. 2012; Schubert et al. 2016; Seager et al. 2020). Here, we instead define meteorological drought as a persistent anomalous precipitation minus evapotranspiration ($P-\mathrm{ET}$) deficit. We take this latter approach because 1) it is the *combined* term $P-\mathrm{ET}$ that provides the atmospheric forcing of a soil moisture deficit and 2) in a quasi-steady state, anomalous $P-\mathrm{ET}$ is balanced by anomalous column-integrated moisture flux convergence (e.g., Trenberth et al. 2011; Newman et al. 2012; Seager and Henderson 2013). Therefore, by focusing on $P-\mathrm{ET}$ deficits, we can more readily relate anomalous atmospheric transport of moisture to anomalous atmospheric forcing of soil moisture. Additionally, column-integrated moisture flux convergence, and hence $P-\mathrm{ET}$, is a more consistent term across different reanalyses than either $P$ or ET alone (e.g., Trenberth et al. 2011; Sebastian et al. 2016).

Regional persistent $P-\mathrm{ET}$ deficits can be connected to large-scale circulation anomalies extending upstream and the remote forcing that triggers these anomalies. For instance, large-scale Rossby wave trains emanating from the tropics and propagating across the North Pacific to North America can engender subseasonal precipitation variability by impacting atmospheric moisture transport (e.g., Schiraldi and Roundy 2017) and have been suggested to potentially affect the Great Plains low-level jet (GPLLJ), the primary atmospheric moisture source for the central United States in the warm season (e.g., Schubert et al. 1998; Weaver and Nigam 2008; Harding and Snyder 2015; Agrawal et al. 2021). Also, extreme weather events on synoptic to subseasonal time scales are sometimes preceded by Rossby wave packets (RWPs), or Rossby waves with limited zonal extent [see, e.g., the review by Wirth et al. (2018)]. For example, during the 1988 U.S. drought, two RWPs forced in Southeast Asia and the western North Pacific led to the development of persistent

anomalous ridges over North America in late May and mid-June, leading to extreme heat wave events and therefore accelerating the drought conditions (e.g., Lyon and Dole 1995; Chen and Newman 1998; Wang et al. 2017).

One of the major challenges in studying large-scale springtime climate variability is the rapid seasonal change in the Rossby waveguide. In mid-May, the subtropical North Pacific jet moves poleward, weakens, and becomes narrower, constraining the waveguide to a narrow region in the extratropics (e.g., Newman and Sardeshmukh 1998; Hoskins and Hodges 2019; Breeden et al. 2021). This change in the Rossby waveguide increases the stationary wavenumber across the North Pacific from early to late spring (e.g., Hoskins and Ambrizzi 1993; Newman and Sardeshmukh 1998), further affecting how large-scale Rossby waves modulate downstream hydroclimatic variability over North America. Consequently, we might need to diagnose early and late spring periods separately to clearly identify the role of intraseasonal variability in persistent $P-\mathrm{ET}$ deficits and subsequent drought development.

In this study, we use reanalysis precipitation and evapotranspiration to examine the recurring features of atmospheric forcing accompanying persistent $P-\mathrm{ET}$ deficits, addressing the atmosphere's role in driving subseasonal drought development in the central United States in early (1 April–15 May) versus late (16 May–30 June) spring. First, following previous work on persistent atmospheric anomalies (e.g., Dole and Gordon 1983; Miller et al. 2020), we categorize persistent $P-\mathrm{ET}$ deficits based on the frequency of their varying spatial distributions, intensities, and durations. This allows for objective characterization of both persistent $P-\mathrm{ET}$ deficits and their associated large-scale circulation anomalies, including remote teleconnections. We also examine the relationship between these persistent $P-\mathrm{ET}$ deficits and corresponding soil moisture anomalies, which we find has a connection to flash drought onset. The rest of the paper is organized as follows. In section 2, reanalysis dataset and soil moisture products are detailed. Section 3 briefly introduces the atmospheric moisture budget used to diagnose observed atmospheric moisture deficits. In section 4, we assess the statistics of persistent $P-\mathrm{ET}$ deficits, from which we specify the regions and thresholds to define our events. Section 5 focuses on the evolutions of persistent $P-\mathrm{ET}$ deficits and the associated atmospheric circulation anomalies. The impacts of persistent $P-\mathrm{ET}$ deficits on soil moisture anomalies are also examined in this section. A summary and concluding remarks are presented in section 6.

## 2. Data

Observed analyses for April–June 1958–2018 are drawn from the 55-yr Japanese Reanalysis Project (JRA-55; Kobayashi et al. 2015). JRA-55 provides 6-hourly atmospheric and land surface diagnostic fields at a $1.25^\circ \times 1.25^\circ$ horizontal resolution. JRA-55 data is also available at 3-h increments at the same horizontal resolution for two-dimensional forecast fields, including the total precipitation and evaporation variables combined in this study as $P-\mathrm{ET}$. The evaporation variable from the JRA-55 forecast fields represents the moisture flux entering the atmosphere from below and is therefore equivalent to evapotranspiration over the land area (Japan Meteorological Agency 2021, personal communication). We also confirmed that $P-\mathrm{ET}$ and the atmospheric moisture budget are well balanced within the JRA-55. Thus, we used $P-\mathrm{ET}$ to characterize meteorological droughts throughout this study. All variables were daily averaged and then smoothed with a 5-day running mean; all analyses in this paper used this smoothed data. A 1958–2018 daily climatology was calculated from each 5-day running mean field.

Land analyses in JRA-55 were conducted using an offline land model [the Japan Meteorological Agency Simple Biosphere Model (JMA SiB); Sellers et al. 1986; Sato et al. 1989] forced by the atmospheric reanalysis every 3 h. JRA-55 has three soil layers whose depths vary with vegetation types (Li et al. 2020). Over the United States east of the Appalachian Mountains, the depths of these three layers are generally 2, 148, and 200 cm. For the Great Plains, a transition zone between wet and dry climates, the depths of each layer are approximately 2, 47, and 100 cm (JMA 2014). For all the regions evaluated in this paper, we used the top two layers to represent the "root zone," the layer with the highest seasonal variability that typically extends from 0 to 40 cm (e.g., Zeng 2001; Ghannam et al. 2016).

JRA-55 soil moisture was compared to soil moisture from an offline simulation of the Community Land Model version 4.5 (CLM; Oleson et al. 2013). This simulation of CLM was integrated at $0.5^\circ \times 0.5^\circ$ horizontal resolution and with 10 fixed layers in the vertical to about 3-m depth. The simulation of CLM was forced by analyses of observed temperature and precipitation from the Climatic Research Unit (CRU) version 3.2–National Centers for Environmental Prediction (NCEP) dataset (CRUNCEP; Viovy and Ciais 2011). We used the top five layers (to 36.6-cm depth) to represent the CLM root zone. Precipitation and evapotranspiration ($P-\mathrm{ET}$) from CLM were also compared to that of JRA-55.

## 3. Atmospheric moisture budget

The atmospheric moisture budget is used to diagnose persistent atmospheric moisture deficits. The conservation of water vapor within an atmospheric column can be written in flux form in pressure ($p$) coordinates, integrated from the surface pressure $p_s$ to the top of the atmosphere (e.g., Peixoto and Oort 1992), as

$$P-\mathrm{ET} = -\frac{1}{g\rho_w}\int_0^{p_s}\frac{\partial q}{\partial t}\,dp - \frac{1}{g\rho_w}\nabla\cdot\int_0^{p_s}\mathbf{V}q\,dp, \qquad (1)$$

where $g$ is Earth's gravitational constant, $\rho_w$ is the density of water vapor, $q$ is specific humidity, and $\mathbf{V}$ is the horizontal wind velocity; $P$ and ET are precipitation and evapotranspiration at the surface, respectively. Equation (1) states that $P-\mathrm{ET}$ is balanced by the column-integrated moisture tendency and the convergence of column-integrated moisture flux.

Bringing the divergence operator into the vertical integral of the last term in Eq. (1) yields

$$-\frac{1}{g\rho_w}\nabla\cdot\int_0^{p_s}\mathbf{V}q\,dp = -\frac{1}{g\rho_w}\int_0^{p_s}\nabla\cdot(\mathbf{V}q)dp - \frac{1}{g\rho_w}q_s\mathbf{V}_s\cdot\nabla p_s. \qquad (2)$$

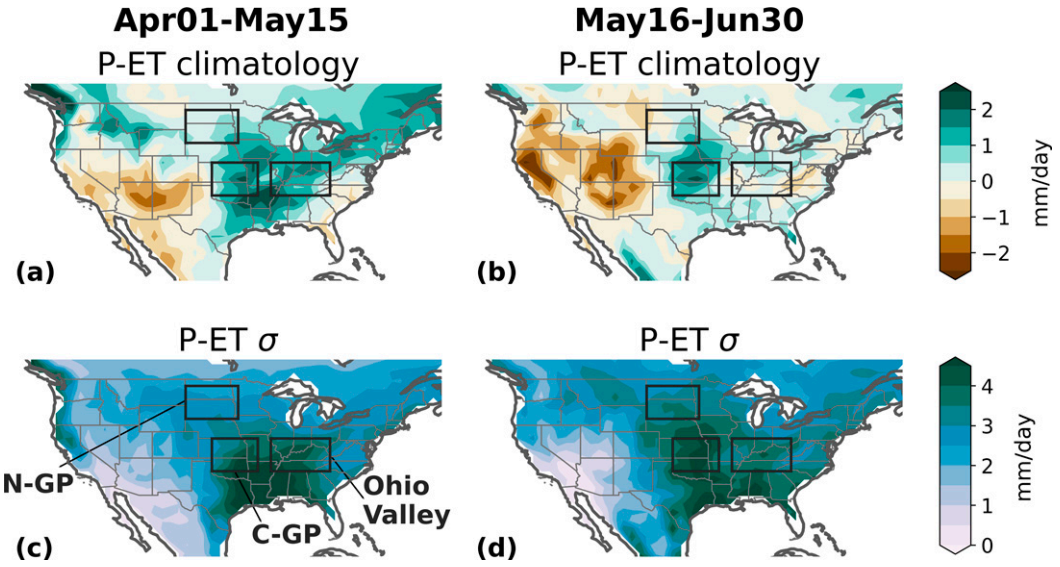


FIG. 1. JRA-55 daily $P-\mathrm{ET}$ (top) climatological mean and (bottom) standard deviation ($\sigma$) in (a),(c) early and (b),(d) late spring. Boxes indicate the three regions used in this study: Ohio Valley (91°–82°W, 35°–40°N), C-GP (100°–93°W, 35°–40°N), and N-GP (104°–96°W, 43°–48.5°N).

The second term on the right-hand side of Eq. (2) is a boundary term that is often neglected [see details in Seager and Henderson (2013)]. The column-integrated divergence of moisture flux, the first right-hand side term of Eq. (2), can be separated into two components by vector identity. Thus, in this study, we approximate the convergence of column-integrated moisture flux by

$$-\frac{1}{g\rho_w}\nabla\cdot\int_0^{p_s}(\mathbf{V}q)dp \approx -\frac{1}{g\rho_w}\int_0^{p_s}(q\nabla\cdot\mathbf{V})dp - \frac{1}{g\rho_w}\int_0^{p_s}\mathbf{V}\cdot\nabla q dp. \quad (3)$$

The first term on the right side of Eq. (3) represents moisture gain due to net mass convergence of moisture into the column. This term is dominated by convergence at low levels, since specific humidity decreases with height. For example, in the presence of strong subsidence, where mass conservation implies upper-level convergence and lower-level divergence, we can expect upper-level convergence of moisture into the column to be outweighed by lower-level divergence of moisture out of the column, resulting in a net drying (e.g., Seager and Henderson 2013). To emphasize this point, we will call this term the subsidence term. The second term on the right-hand side of Eq. (3) represents moistening due to moisture advection, typically positive for southerly winds bringing moisture from wetter regions to the south. We call this term the advection term.

## 4. Determining criteria for persistent $P-\mathrm{ET}$ deficit composites

In this section, we examine the behavior of persistent $P-\mathrm{ET}$ deficit anomalies in terms of their regionality, intensity, and duration in early and late spring. Based upon this behavior, we determine the criteria used to select events that make up the drought composites discussed in the following sections.

### *a. Selection criteria for regions*

During spring, the central United States receives 30%–45% of its annual precipitation and experiences maximum $P-\mathrm{ET}$ variability (e.g., Wang and Chen 2009; Mo 2011; Agrawal et al. 2021). However, for different regions this springtime maximum occurs during either early or late in the season, as illustrated by Fig. 1, which presents the mean and standard deviation of $P-\mathrm{ET}$ over the United States for each half of the spring season. In early spring, $P-\mathrm{ET}$ is large across a broad region within the central United States, from the Great Plains extending to the Ohio River Valley and the Lower Mississippi River Basin (Fig. 1a). In late spring, positive values are mostly confined to the central Great Plains region (Fig. 1b), with large areas of the country apparently acting as a mean *source* of moisture [i.e., $P-\mathrm{ET}<0$ as in Newman et al. (2012)].

Motivated by spatial variations of $P-\mathrm{ET}$ climatology and the location of notable springtime subseasonal droughts (Table 1), we selected three regions within the broad central United States (indicated in Fig. 1 and listed in Table 2): 1) the Ohio Valley, where some of the most severe central U.S. droughts over the recent decades occurred, including the 1980, 1988, and 2012 droughts; 2) the central Great Plains (C-GP), one of the most susceptible regions to warm season drought in the United States, including the Dust Bowl in the 1930s, the extended drought in the 1950s (e.g., Cook et al. 2011), and many subseasonal-to-seasonal springtime droughts during our study period; and 3) the northern Great Plains (N-GP), which experienced the 2017 northern Great Plains flash drought in early May 2017. We constructed indices from area-averaged $P-\mathrm{ET}$ anomalies within each box, where each

TABLE 2. The thresholds of intensity and duration used to select persistent $P-$ ET deficits events for each region (indicated in Fig. 1). The table also includes the onset dates of all selected events in early (1 Apr–15 May) and late (16 May–30 Jun) spring in each region, whose geographical domain is also indicated. The numbers of events for each subset are shown in the parentheses.

| Ohio Valley | | Central Great Plains (C-GP) | | Northern Great Plains (N-GP) | |
|---|---|---|---|---|---|
| 91°–82°W, 35°–40°N<br>Intensity: ≤−1 std<br>Duration: at least 8 days | | 100°–93°W, 35°–40°N<br>Intensity: ≤−1 std<br>Duration: at least 7 days | | 104°–96°W, 43°–48.5°N<br>Intensity: ≤−1 std<br>Duration: at least 7 days | |
| Early (14) | Late (13) | Early (11) | Late (18) | Early (14) | Late (10) |
| 8 Apr 1960 | 28 May 1966 | 5 May 1962 | 6 Jun 1959 | 28 Apr 1968 | 23 May 1968 |
| 20 Apr 1962 | 21 Jun 1966 | 28 Apr 1968 | 28 Jun 1963 | 11 May 1973 | 21 Jun 1970 |
| 15 May 1962 | 9 Jun 1967 | 12 May 1973 | 17 May 1964 | 25 Apr 1977 | 8 Jun 1973 |
| 4 May 1963 | 21 May 1970 | 26 Apr 1987 | 26 May 1966 | 20 Apr 1980 | 23 Jun 1973 |
| 1 May 1965 | 30 Jun 1970 | 10 May 1987 | 30 Jun 1970 | 15 Apr 1987 | 14 Jun 1974 |
| 11 Apr 1971 | 19 May 1972 | 7 May 1988 | 2 Jun 1972 | 8 May 1987 | 6 Jun 1978 |
| 5 Apr 1976 | 2 Jun 1984 | 3 May 1992 | 20 Jun 1974 | 10 Apr 1988 | 25 May 1983 |
| 10 Apr 1977 | 16 Jun 1986 | 12 Apr 2006 | 4 Jun 1976 | 28 Apr 1992 | 19 Jun 1988 |
| 12 May 1977 | 29 May 1988 | 14 May 2006 | 4 Jun 1977 | 13 May 1993 | 16 Jun 2008 |
| 2 May 1980 | 17 Jun 2005 | 20 Apr 2012 | 11 Jun 1978 | 9 May 1997 | 29 Jun 2013 |
| 28 Apr 1981 | 21 May 2007 | 12 May 2012 | 9 Jun 1980 | 15 May 2006 | |
| 1 Apr 1995 | 31 May 2011 | | 7 Jun 1988 | 27 Apr 2007 | |
| 27 Apr 2001 | 22 Jun 2012 | | 19 May 1994 | 11 May 2012 | |
| 30 Apr 2015 | | | 15 Jun 1995 | 6 May 2017 | |
| | | | 21 Jun 2002 | | |
| | | | 22 Jun 2005 | | |
| | | | 26 Jun 2012 | | |
| | | | 6 Jun 2016 | | |

box is sized so that the correlation between the index and $P-$ ET anomalies at each grid point within the box is everywhere above 0.7. All three selected regions have relatively high $P-$ ET variability within the central United States during either early or late spring (Fig. 1, bottom panels).

### b. *Selection thresholds for intensity and duration of persistent $P-$ ET deficits*

Two-dimensional cumulative histograms of intensity and duration for $P-$ ET anomalies in each region, also called intensity–duration–frequency diagrams, are used to identify subseasonal meteorological droughts (Fig. 2). Our analysis followed the approach taken in studies of persistent anomalies in different meteorological or oceanographic contexts, which leveraged similar intensity–duration–frequency relationships to define events such as atmospheric blocking (e.g., Dole and Gordon 1983; Miller et al. 2020) and marine heat waves (e.g., Scannell et al. 2016; Xu et al. 2021). In this study, we similarly defined a *persistent* $P-$ ET *deficit* as an extended period of dry (negative) $P-$ ET anomalies. The onset date of a single $P-$ ET deficit event is the time at which the magnitude of the negative $P-$ ET anomaly first rises above a specified threshold, whose intensity is measured in units of standard deviation (std) of $P-$ ET, calculated separately for early and late spring. The event duration is then the number of days that the $P-$ ET deficit remains above the intensity threshold for that event. The statistics of all such persistent $P-$ ET deficit events are gathered to produce Fig. 2, which shows the cumulative frequency (shading) of events for varying values of intensity (ordinate) and duration (abscissa). For example, the value plotted for 1.0 std intensity and 7-day duration represents the cumulative frequency of all events for which persistent $P-$ ET deficits are equal to or greater than one standard deviation and persist for at least seven days.

Details of the intensity–duration–frequency plots are broadly similar across the three regions and between both subseasons. Frequency generally declines monotonically with increasing intensity and duration. Still, there are a few notable differences. For the Ohio Valley (Fig. 2, left panels), $P-$ ET deficits of a given intensity persisted slightly longer in late spring than in early spring. In the C-GP (Fig. 2, central panels), $P-$ ET deficits also tended to persist longer in late spring than in early spring, given the same intensity threshold. In contrast, $P-$ ET deficits in the N-GP (Fig. 2, right panels) tended to persist longer in early spring compared to late spring, especially for events with greater intensity.

The frequency of occurrence does not show a dependence upon either intensity or duration that would clearly distinguish extreme from nonextreme events. That is, using any pair of intensity and duration values to define an "extreme" event appears to be inherently arbitrary, with a trade-off between increasing the event sample size on the one hand and capturing particularly extreme (in intensity and/or duration) events on the other. Therefore, to define persistent $P-$ ET deficit events, we chose a pair of intensity and duration thresholds corresponding to a frequency of 0.5%, which yielded at least 10 events for each region in each subseason. We have tested the sensitivity of our results based upon different thresholds

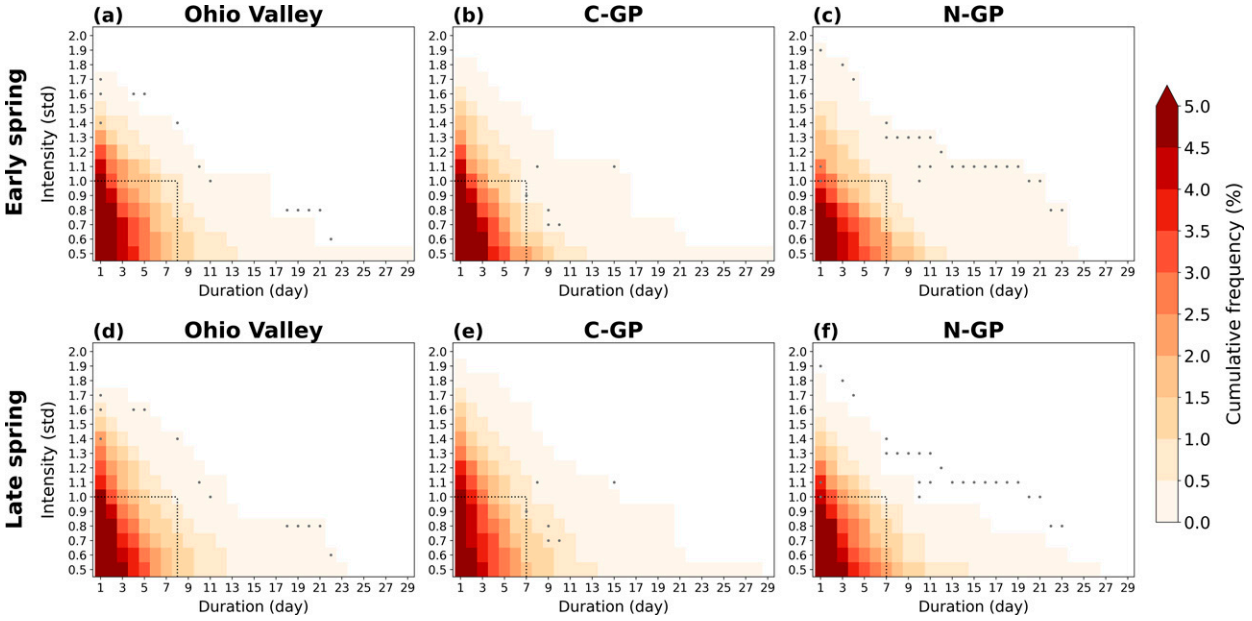


FIG. 2. Intensity–duration–frequency diagrams of $P-$ ET deficits over the (left) Ohio Valley, (center) C-GP, and (right) N-GP, defined by black boxes in Fig. 1, in (a)–(c) early and (d)–(f) late spring. The ordinate presents the intensity of negative $P-$ ET anomalies in terms of standard deviation (std) of daily $P-$ ET across each subseason. The abscissa shows the duration (days) of $P-$ ET deficits that exceed a certain intensity. Shading displays the cumulative frequency of $P-$ ET deficit anomalies for different combinations of intensity and duration during 1958–2018. Dotted lines indicate the criteria for selecting persistent $P-$ ET deficits events for each region used in this study. The complete information of the criteria and lists of the events are presented in Table 2. Black dots denote that the differences in frequency between early and late spring are significantly different from each other.

for intensity and duration and found that the results were qualitatively insensitive to these choices (not shown). The criteria (thresholds for duration and intensity) are different for each region but are fixed for both early and late spring. The thresholds and sample sizes for each region, along with the onset dates of the events, are included in Table 2.

### c. Composites and statistical significance

Composites were constructed for each region during each subseason, averaging across the events whose onset dates were listed in Table 2. The statistical significance of composites was assessed using Monte Carlo resampling. First, the onset dates were randomly chosen in the spring season based on the same sample size of selected persistent $P-$ ET deficits events in each subseason and region. By compositing the variables for randomly selected days and repeating the procedure 1000 times, we could approximate the distribution of the sample mean and subsequently assess the significance of the targeted composites. We separately tested whether composite anomalies and/or differences between early and late spring composites were significantly different from zero at the 95% confidence level, based on this bootstrapping method.

## 5. Evolution of persistent $P-$ ET deficits and associated anomalies

In this section, we examine the composite evolution of large-scale circulation anomalies related to persistent $P-$ ET deficits in the three central U.S. regions during early and late spring. We begin by considering the Ohio Valley region, and then compare to the C-GP and N-GP regions. The composite evolution of soil moisture anomalies is also investigated at the end of this section.

### a. Ohio Valley

We first demonstrate how seasonality may impact the structure of the wave train arcing across the North Pacific–North America (NP-NA) region, by correlating Northern Hemisphere 300-hPa meridional wind upon Ohio Valley $P-$ ET, for the entire spring season (Fig. 3, top panels) and separately for both early (Fig. 3, middle panels) and late (Fig. 3, bottom panels) spring. In early spring, five days prior to the Ohio Valley $P-$ ET target (lag $-5$), a wave train emanates from east of Japan to North America (Fig. 3c). Five days later (at lag 0), the wave train's centers of maximum amplitude have propagated considerably eastward across North America into the Atlantic, albeit with little phase propagation (Fig. 3d). In late spring (Fig. 3e), the Ohio Valley $P-$ ET is again related to a wave train originating near Japan, spanning the North Pacific to reach North America. However, the scale of this wave train is smaller than in early spring, with the late spring wave train having one more center and being more meridionally confined to the 40°–60°N band. These differences are consistent with the Rossby waveguide changing over the course of the spring season, with both a weaker and narrower jet in late spring (cyan lines in Fig. 3), resulting in a reduction

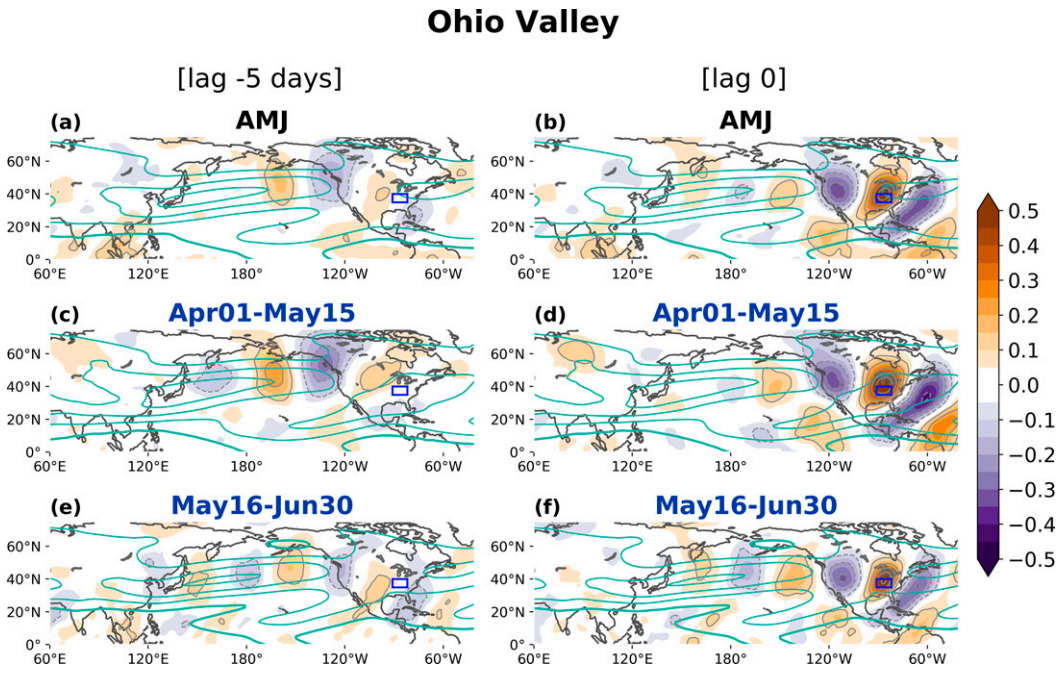


FIG. 3. Correlation between Ohio Valley $P$ − ET and 300-hPa meridional wind during (a),(b) 1 Apr–30 Jun, (c),(d) 1 Apr–15 May, and (e),(f) 16 May–30 Jun. (right) The autocorrelation between the two variables, and (left) the lag correlation: $P$ − ET lags meridional wind for 5 days. The $P$ − ET is averaged over the Ohio Valley region shown in Fig. 1 and indicated by blue boxes. Gray lines are drawn at 0.1 correlation intervals. Cyan contours depict the climatological 300-hPa zonal wind in each corresponding period with intervals of 10 m $s^{-1}$. Thick solid lines indicate climatological 0 m $s^{-1}$ isotach.

in the spatial scales of stationary Rossby waves (e.g., Newman and Sardeshmukh 1998).

The reduction of the Rossby wave scale from early to late spring supports the separation of the springtime analysis into two subseasons. Moreover, when we repeat the correlation analysis over the entire spring season (Fig. 3, top panels), the Ohio Valley $P-$ET appears related to a local wave train emanating from the *eastern* North Pacific five days prior to the Ohio Valley $P-$ET anomaly peak (Fig. 3a). The wave train subsequently intensifies with little downstream propagation (Fig. 3b). That is, if the spring season were treated as a whole, the distinct upstream teleconnection patterns in early and late spring would be mispresented, the result of averaging two Pacific wave trains that are not in phase.

The composite anomalies related to persistent $P-$ET deficits over the Ohio Valley, shown in Fig. 4, also appear to be associated with large-scale Rossby waves whose spatial scale changes from early to late spring. In early spring, both upper-level geopotential height and lower-level meridional wind anomalies (see Hovmöller diagrams of Figs. 4c,d) include a Rossby wave packet (RWP) appearing to originate from the western North Pacific about 10 days before the onset of the composite persistent $P-$ET deficits. While the waves within the RWP are quasi-stationary, the RWP itself has a pronounced eastward group velocity across the North Pacific, reaching North America two days before the $P-$ET deficit onset (Figs. 4a,c). The slow phase propagation of the individual troughs and ridges within the RWP allows for persistent surface anomalies to develop over the Ohio Valley. The picture is broadly similar in late spring, when again a quasi-stationary RWP propagates across the NP-NA sector (Figs. 4g,h), with the arrival of a high-amplitude quasi-stationary RWP over the Ohio Valley region leading to a $P-$ET deficit there. However, this RWP shows less phase propagation and statistically significantly narrower horizontal scale than the RWP during early spring (cf. Figs. 4g and 4c). As a result, the persistent $P-$ET deficits are more localized in the region in late spring than in early spring (cf. Figs. 4e and 4a).

To explore the potential forcing that might trigger the quasi-stationary RWPs, we next examine the composites of anomalous column-integrated diabatic heating and 300-hPa geopotential height for the persistent $P-$ET deficits (Fig. 5). In early spring (Fig. 5, left panels), a dipole of convective anomalies persists across the tropical western Pacific from 10 days before the onset, but both have limited areal extent. In late spring (Fig. 5, right panels), small-scale and transient heating anomalies are again located upstream of the RWP in the western tropical Pacific. While there are statistically significant upstream diabatic heating sources present for both early and late spring, it is unclear what role (if any) they have in forcing the downstream RWPs.

In both early and late spring, the quasi-stationary RWP induces an anomalous ridge located west of the Ohio Valley,

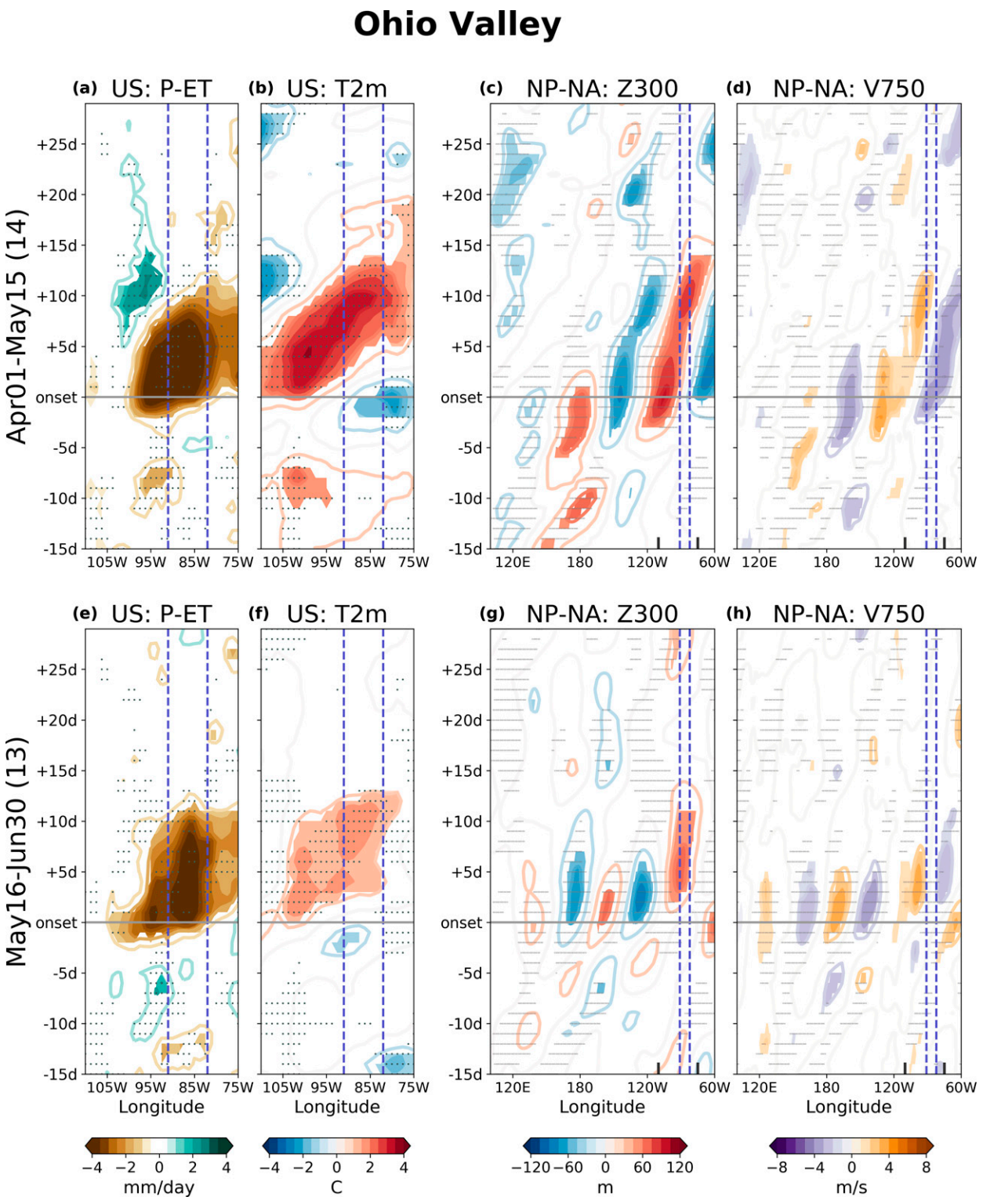


FIG. 4. Hovmöller diagrams for the composite persistent $P-\mathrm{ET}$ deficit events for the Ohio Valley region. (a),(e) $P-\mathrm{ET}$ (mm day$^{-1}$) and (b),(f) 2-m air temperature (T2m; °C) over the United States and (c),(g) 300-hPa geopotential height (Z300; m) and (d),(h) 750-hPa meridional wind (V750; m s$^{-1}$) anomalies across the NP-NA region in (top) early and (bottom) late spring. For $P-\mathrm{ET}$ and T2m, the anomalies are averaged over the 35°–40°N (see the Ohio Valley box in Fig. 1). The anomalies of Z300 and V750 are averaged over 35°–55°N. Purple dashed lines indicate the longitudinal range of the Ohio Valley area defined in Fig. 1 and Table 2. The longitudinal range for the United States in the left two columns is also labeled in the right two columns (black ticks). The statistically significant anomalies are shaded. Dots represent that the differences between early and late spring are statistically significant.

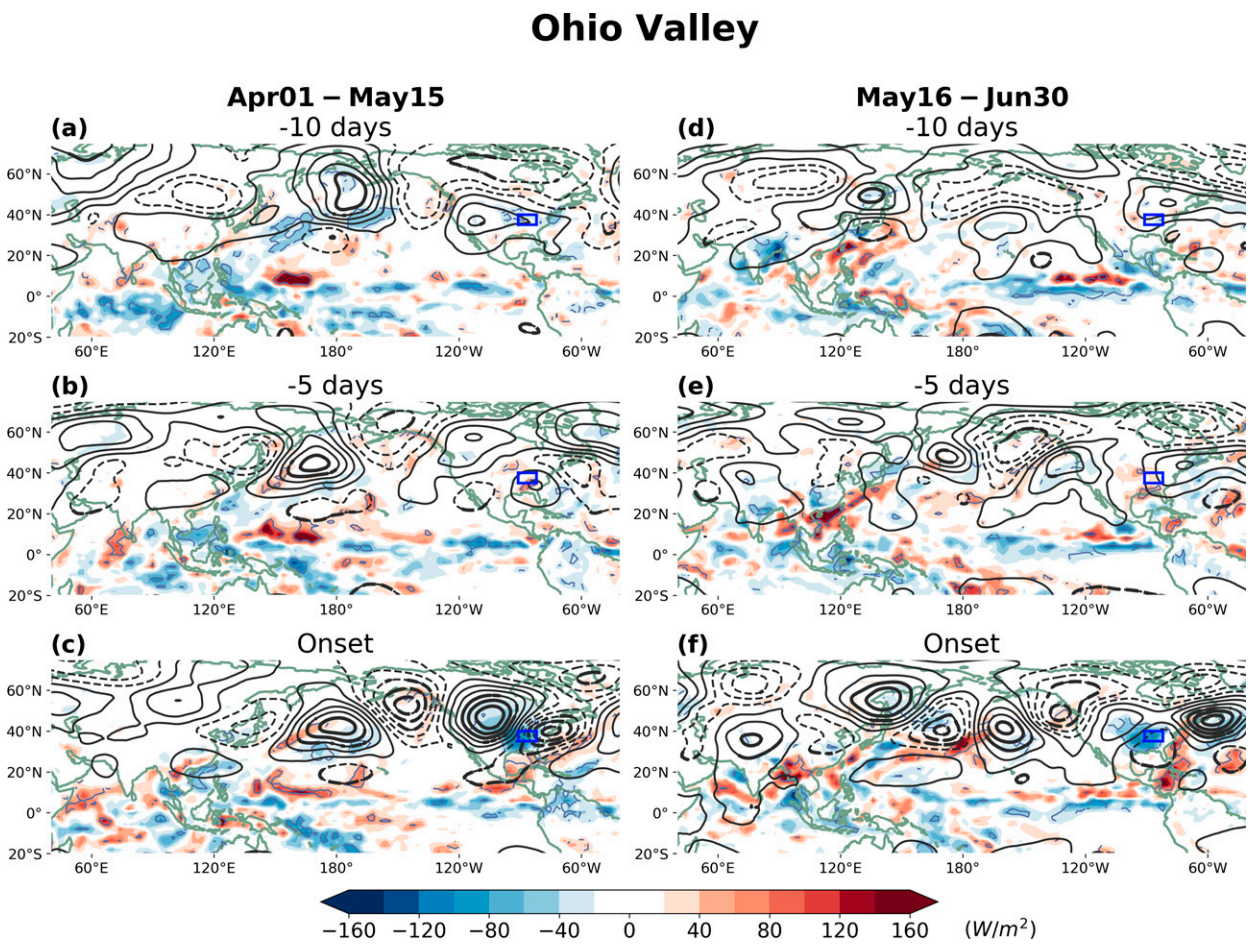


FIG. 5. Composites of JRA-55 300-hPa geopotential height (contours; interval: 20 m), and column-integrated diabatic heating (shading; W $m^{-2}$) anomalies for the Ohio Valley persistent $P-ET$ deficit events in (a)–(c) early and (d)–(f) late spring, at (top) 10 days prior to the onset, (middle) 5 days prior to the onset, and (bottom) the onset. Thick lines indicate that Z300 anomalies are statistically significant. For column-integrated diabatic heating, the anomalies that significantly differ from zero are encompassed by thin gray lines.

as well as a downstream trough that is considerably stronger in early spring (Figs. 4 and 5). At the onset of the persistent $P-ET$ deficits, the ridge has a largely equivalent barotropic vertical structure with a slight northwestward tilt (Fig. 6, top panels, cf. black and green contours). Negative vorticity advection drives strong subsidence downstream of this ridge (Fig. 6, top panels), following the quasigeostrophic omega equation. The subsidence corresponds with low-level divergent flow (which may be inferred from the arrows in the bottom panels of Fig. 6) and strong local drying of the mid-to-lower troposphere, within and to the south of the Ohio Valley region (Fig. 6, bottom panels, shading).

Examination of the atmospheric moisture budget (Fig. 7) shows that this atmospheric drying over the Ohio Valley (see also Fig. 7, middle panels) may be primarily attributed to the strong subsidence seen in Fig. 6 and its corresponding impact on column-integrated moisture flux convergence via the subsidence term in Eq. (3) (purple dashed lines, Fig. 7, bottom panels) rather than to reduced moisture advection (pink dotted lines) arising from the anomalous low-level northerlies (Fig. 7, middle panels). In fact, apart from atmospheric drying (i.e., the negative moisture tendency), negative $P-ET$ anomalies are largely balanced by the subsidence term, with both having increased amplitude starting about three days prior to the onset of the event (cf. green solid and purple dashed lines in Fig. 7, bottom panels), for both early and late spring. This rough balance continues throughout the course of the persistent $P-ET$ deficits, suggesting that these meteorological droughts are driven by strong subsidence rather than anomalous dry advection into the region or reduction in the climatological moisture transport from the south.

It is particularly noteworthy that Ohio Valley persistent $P-ET$ deficits are not preceded by local warm temperature anomalies (Fig. 4, left two columns), either in early or late spring, suggesting that these moisture deficits are not initiated by enhanced evapotranspiration related to above-average temperatures. Instead, the warm temperature anomalies largely occur after the maximum $P-ET$ deficit, concurrent

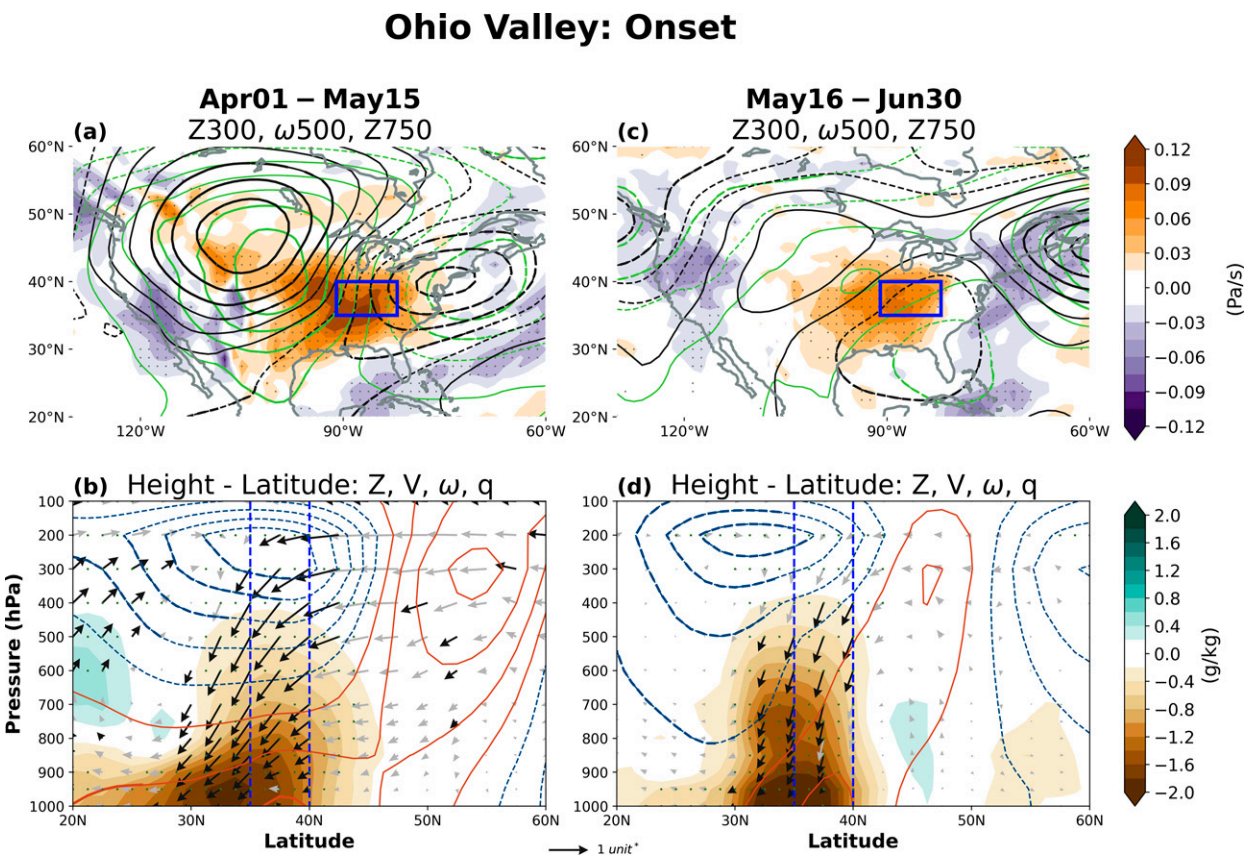


FIG. 6. Vertical structure of the anomalous circulations. (top) Composites of 300-hPa geopotential height (black contours; interval: 20 m), 500-hPa vertical velocity (shading; Pa $s^{-1}$), and 750-hPa geopotential height (green contours; interval: 10 m) anomalies for the Ohio Valley persistent $P-$ ET deficit events in (a) early and (c) late spring at the onset. Thick lines indicate that Z300 and Z750 anomalies are statistically significant. Dots denote that $\omega$500 anomalies are statistically significant. (bottom) Composite vertical–latitude cross sections of geopotential height (contours; interval: 10 m), specific humidity (shading; g $kg^{-1}$), meridional wind and vertical velocity (arrows) averaged over 91°–82°W (see the Ohio Valley box; Table 2) in (b) early and (d) late spring at the onset of the persistent $P-$ET deficit events. For visualization purposes, vertical velocity is scaled by $-100$. Thus, one unit of the arrow is equivalent to $1\sqrt{[V\ (\mathrm{m\ s^{-1}})]^2+[-100\omega\ (\mathrm{Pa\ s^{-1}})]^2}$. Thick lines and dots indicate that height and specific humidity anomalies are statistically significant, respectively. Black arrows represent that both meridional wind and vertical velocity anomalies are statistically significant. Bright blue dashed lines indicate the latitudinal range of the Ohio Valley area defined in Table 2.

with local development of anomalous 300-hPa geopotential height (Z300) ridging (Fig. 4, center two columns). Interestingly, the temperature anomalies are much weaker in late spring than in early spring.

### b. C-GP

Similar to those in the Ohio Valley, persistent $P-$ ET deficits over the C-GP are related to RWPs crossing the NP-NA sector (Fig. 8) that show more phase propagation and wider horizontal scale in early than in late spring (cf. Figs. 8c and 8g). There is also a similar pattern of subsidence, which is again more widespread in early than late spring (Figs. 9a,c and Figs. S1a,c in the online supplemental material). The C-GP composite RWP has some key elements in common with wave patterns observed during the onset or intensification of some historical subseasonal droughts in spring in the central Great Plains (see Table 1 for references). In late May 1988, a Rossby wave triggered by convective anomalies over the western tropical Pacific propagated across the NP-NA sector in fewer than five days, resulting in a quasi-stationary wave train with a strong anomalous ridge over north-central North America and an anomalous trough over the southeastern United States, which persisted for over 10 days (e.g., Mo et al. 1991; Chen and Newman 1998; Wang et al. 2017), leading to persistent $P-$ET deficits over the C-GP and Ohio Valley. Similarly, the 2012 Great Plains flash drought was driven by a series of persistent precipitation deficit episodes over the C-GP during May and June. Each of these episodes was embedded within a wave train propagating from the western North Pacific, with the central United States sandwiched between an anomalous ridge and trough (DeAngelis et al. 2020). Thus, our composite analysis has captured some recurring features of NP-NA wave patterns seen during these historical springtime subseasonal droughts.

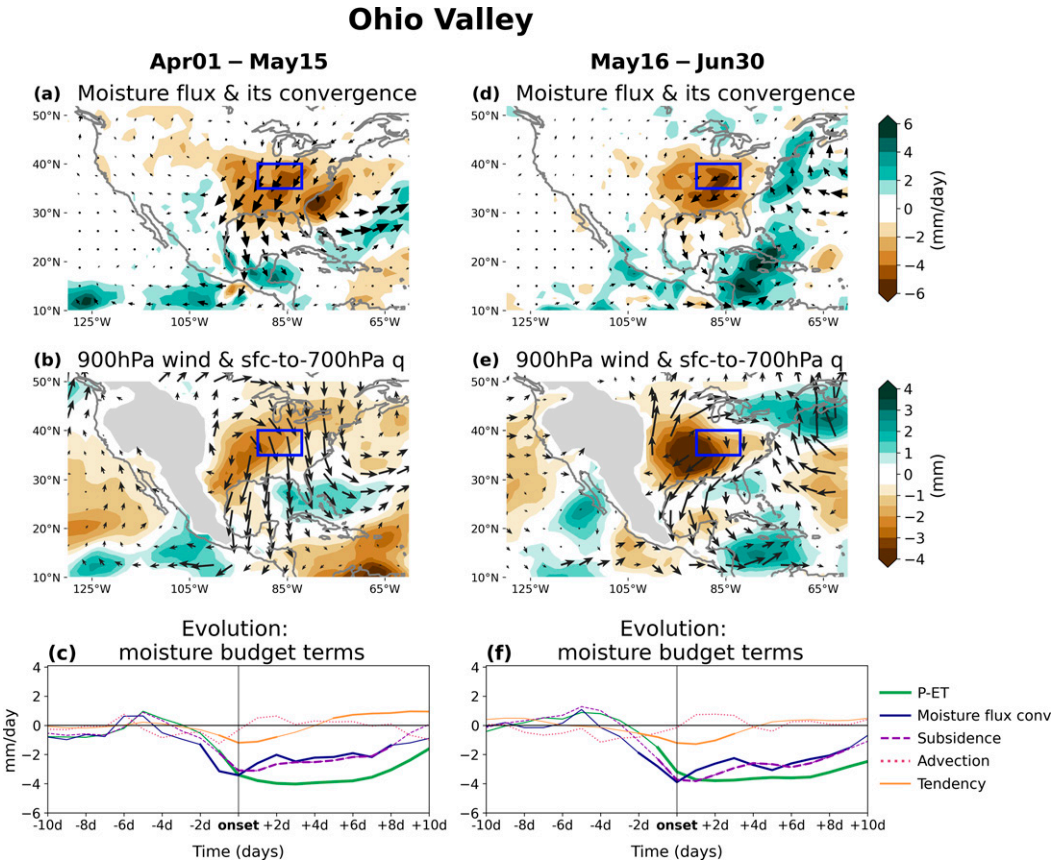


FIG. 7. Composites of (a),(d) anomalous column-integrated moisture flux (arrows) and its convergence (shading; mm day$^{-1}$) and (b),(e) 900-hPa horizontal wind anomalies (arrows) and anomalous low-level moisture (shading; mm) for the Ohio Valley persistent $P-\mathrm{ET}$ deficit events in (a),(b) early and (d),(e) late spring at the onset. In (b) and (e), low-level moisture is specific humidity integrating from surface pressure level to 700 hPa. Regions where surface pressure levels are above 900 hPa are masked out. The region of the Ohio Valley is indicated by the blue boxes. (c),(f) The composite evolution of each term in Eqs. (1) and (3), averaged over the Ohio Valley. Solid lines represent each term in the atmospheric moisture budget [Eq. (1)]: green lines are the anomalous $P-\mathrm{ET}$, navy lines are the anomalous convergence of column-integrated moisture flux, and orange lines are the tendency term. The two components of the convergence of column-integrated moisture flux [Eq. (3)] are shown in purple dashed lines (subsidence term) and pink dotted lines (advection term). The thicker lines denote the anomalies that significantly differ from zero.

The vertical cross sections in Figs. 9a and 9c show that subsidence is again located downstream of the anomalous ridge west of the C-GP (Fig. 8, third column). Similar to the Ohio Valley composite, the atmospheric moisture budget within the C-GP is largely dominated by the local subsidence term (Fig. 10, bottom panels, purple dashed lines). The advection term does play a more important role until about a day before onset in early spring (Fig. 10c, pink dotted line), but in late spring its role is even less than in the Ohio Valley (Fig. 10f). In fact, the $P-\mathrm{ET}$ deficit is almost entirely balanced by the subsidence term in late spring (cf. green solid and purple dashed lines in Fig. 10f), leaving only a relatively small residual drying of the atmospheric column.

Despite the overall similarity of the persistent $P-\mathrm{ET}$ deficits between the C-GP and the Ohio Valley, some regional details are different in late spring. The RWPs related to the C-GP persistent $P-\mathrm{ET}$ deficits are stronger, more stationary, and thus more persistent, compared to the Ohio Valley composite (cf. Figs. 8g and 4g). Also, the concurrent warm temperature anomalies are centered west of the C-GP in late spring (Fig. 8f), distinct from the early spring feature (Fig. 8b) and the Ohio Valley ones (Figs. 4b,f).

### c. N-GP

The general features of the large-scale circulation anomalies related to the N-GP persistent $P-\mathrm{ET}$ deficits resemble those discussed for the Ohio Valley and C-GP: quasi-stationary RWPs across the NP-NA include a persistent anomalous ridge west of the N-GP (Fig. 11) and strong downstream subsidence desiccating the atmospheric moisture over the region (Figs. 9b,d and Figs. S1b,d) in both early and late spring. In fact, individual early spring N-GP and C-GP events are often

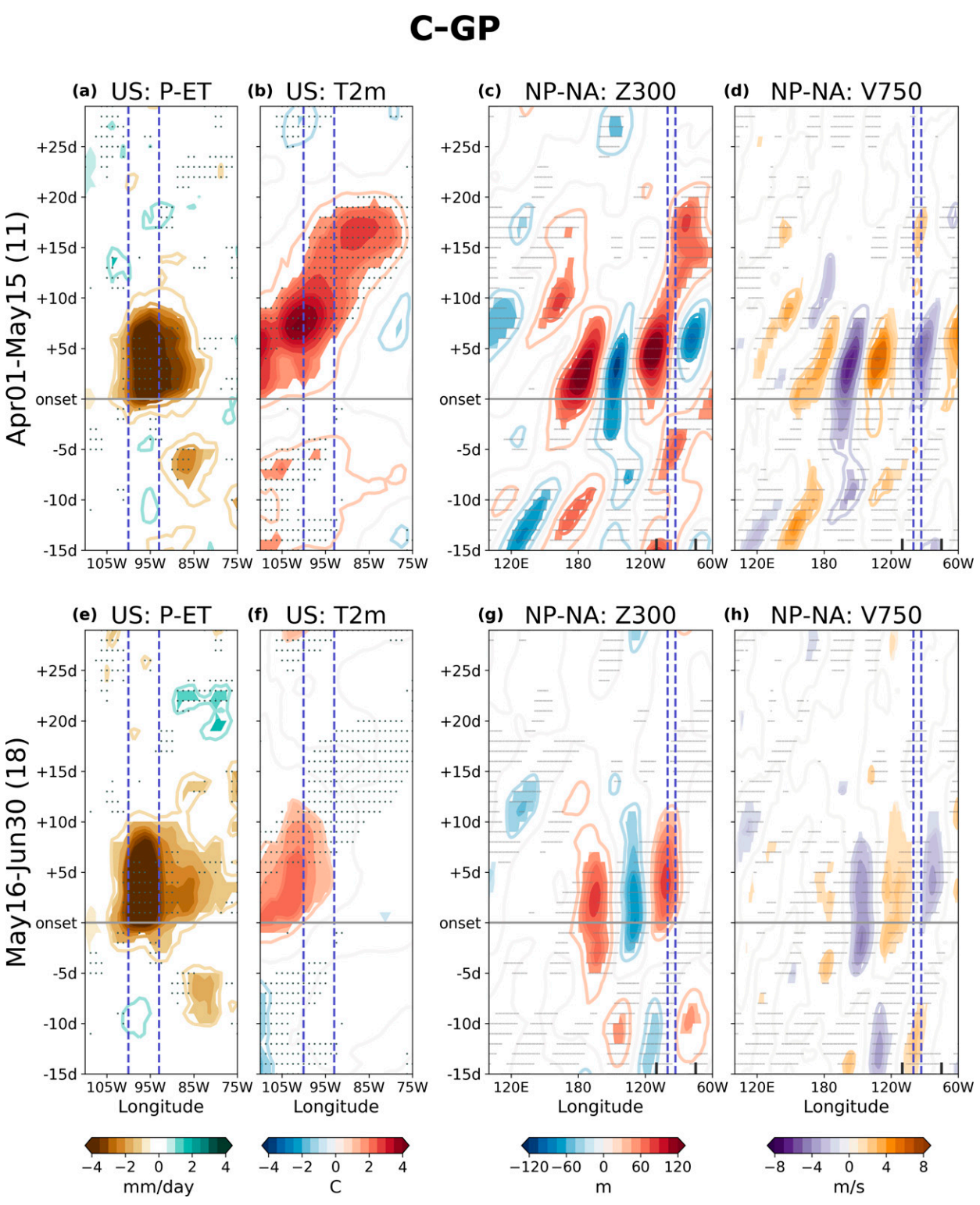


FIG. 8. Hovmöller diagrams for the composite persistent $P-\mathrm{ET}$ deficit events for the C-GP region. (a),(e) $P-\mathrm{ET}$ (mm day$^{-1}$) and (b),(f) T2m (°C) over the United States and (c),(g) Z300 (m) and (d),(h) V750 (m s$^{-1}$) anomalies across the NP-NA region in (top) early and (bottom) late spring. For $P-\mathrm{ET}$ and T2m, the anomalies are averaged over 35°–40°N (see the C-GP box in Fig. 1). The anomalies of Z300 and V750 are averaged over 35°–55°N. Purple dashed lines indicate the longitudinal range of the C-GP area defined in Fig. 1 and Table 2. The longitudinal range for the United States in the left two columns is also labeled in the right two columns (black ticks). The statistically significant anomalies are shaded. Dots represent that the differences between early and late spring are statistically significant.

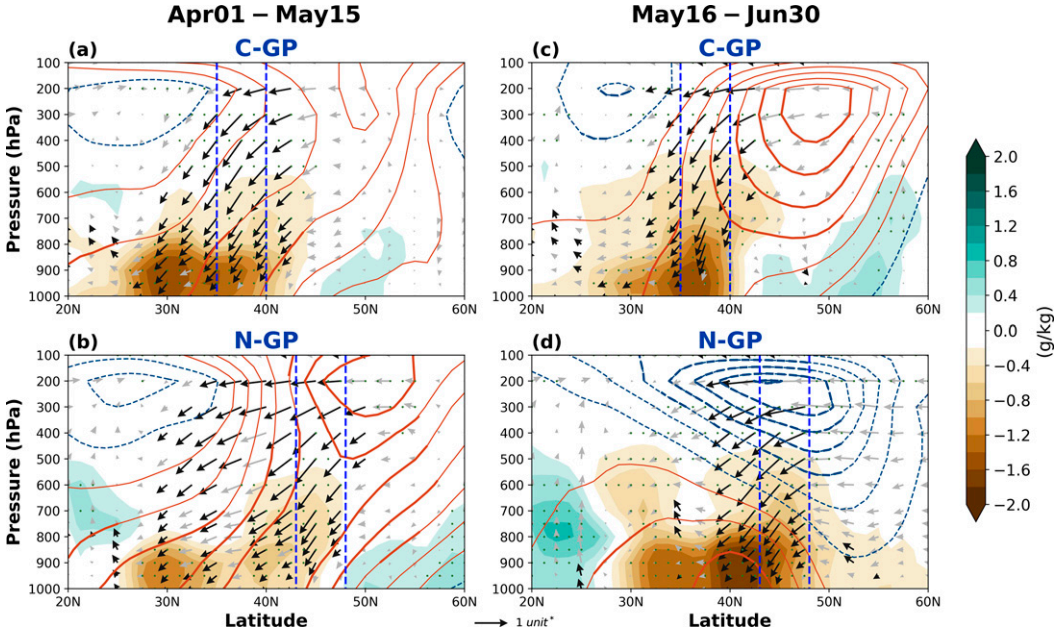


FIG. 9. The composite vertical–latitude cross sections of geopotential height (contours; interval: 10 m), specific humidity (shading; g kg$^{-1}$), meridional wind, and vertical velocity (arrows) averaged over (a),(c) 100°–93°W (C-GP in Table 2) and (b),(d) 104°–96°W (N-GP in Table 2) in (left) early and (right) late spring at the onset of the persistent $P-$ ET deficit events. For visualization purposes, vertical velocity is scaled by −100. Thus, one unit of the arrow is equivalent to $1\sqrt{\left[V\ (\mathrm{m\ s^{-1}})\right]^2+\left[-100\omega\ (\mathrm{Pa\ s^{-1}})\right]^2}$. Thick lines and dots indicate that height and specific humidity anomalies are statistically significant, respectively. Black arrows represent that both meridional wind and vertical velocity anomalies are statistically significant. Bright blue dashed lines indicate the latitudinal range of the C-GP and N-GP area defined in Fig. 1 and Table 2.

influenced by the same wave train extending westward to the date line, so many of the persistent $P-$ ET deficit events in both regions coincide (7 out of 11 early spring C-GP events coincide with N-GP events; see Table 2). This suggests that the spatial scale of the early spring anomalies is large enough to impact both regions simultaneously, with a slight delay due to the RWP propagation. By late spring, on the other hand, with the reduction in the RWP meridional scale, N-GP events no longer arise from the same RWP and are generally not coincident with C-GP (or Ohio Valley) events. This distinct change in the regionality from early to late spring is clearly seen in the vertical structure composites (Fig. 9). In early spring, the circulation and moisture anomalies for the C-GP and N-GP persistent $P-$ ET deficit events have substantially similar vertical structures (Fig. 9, left panels). In late spring, however, while the circulation anomalies for the C-GP events remain largely similar to the early spring one with the anomalous ridge slightly west of the C-GP (Fig. 9c and Fig. S1c), the circulation anomalies for the N-GP events shift westward with the upper-level trough more centered to the N-GP and the ridge located farther west (Fig. 9d and Fig. S1d). Thus, the large-scale circulations responsible for the N-GP events are distinct from the ones for the C-GP events in late spring.

Another dissimilarity in the regionality among the central United States from early to late spring exists in the mean $P-$ ET (Fig. 1, top panels). In early spring, $P$ overwhelms ET in all three regions so that $P-\mathrm{ET}>0$ (Fig. 1a). In late spring, ET overwhelms $P$ over the N-GP (Fig. 1b), and this region acts as a mean source of moisture (i.e., $P-\mathrm{ET}<0$). This would matter if we define meteorological droughts based on persistent $P$ deficits as many previous studies have done, rather than on $P-$ ET deficits. The composite relationship between $P$ deficits, near-surface temperature anomalies, and large-scale circulation over the Ohio Valley and C-GP (not shown) is similar to the one based on $P-$ ET deficits (Figs. 4 and 8), although the events are not exactly the same, with some events more dominated by enhanced ET that would be left out. On the other hand, for the N-GP, in early spring, the persistent $P$ deficits are still clearly related to RWPs across the NP-NA, although the number of events drops to only six (Fig. S3, top panels). Nevertheless, in late spring, the relationship among $P$ deficits, temperature anomalies, and circulation anomalies (Fig. S3, bottom panels) displays very different features from the ones based on $P-$ ET deficits (Fig. 11, bottom panels), demonstrating the importance of ET in driving meteorological drought over the N-GP in late spring and a distinct regionality among the central United States compared to the early spring one.

### *d. Evolution of anomalous root zone soil moisture related to the persistent $P-$ ET deficits*

For all three central U.S. regions examined, persistent $P-$ ET deficits arise largely due to strong subsidence related

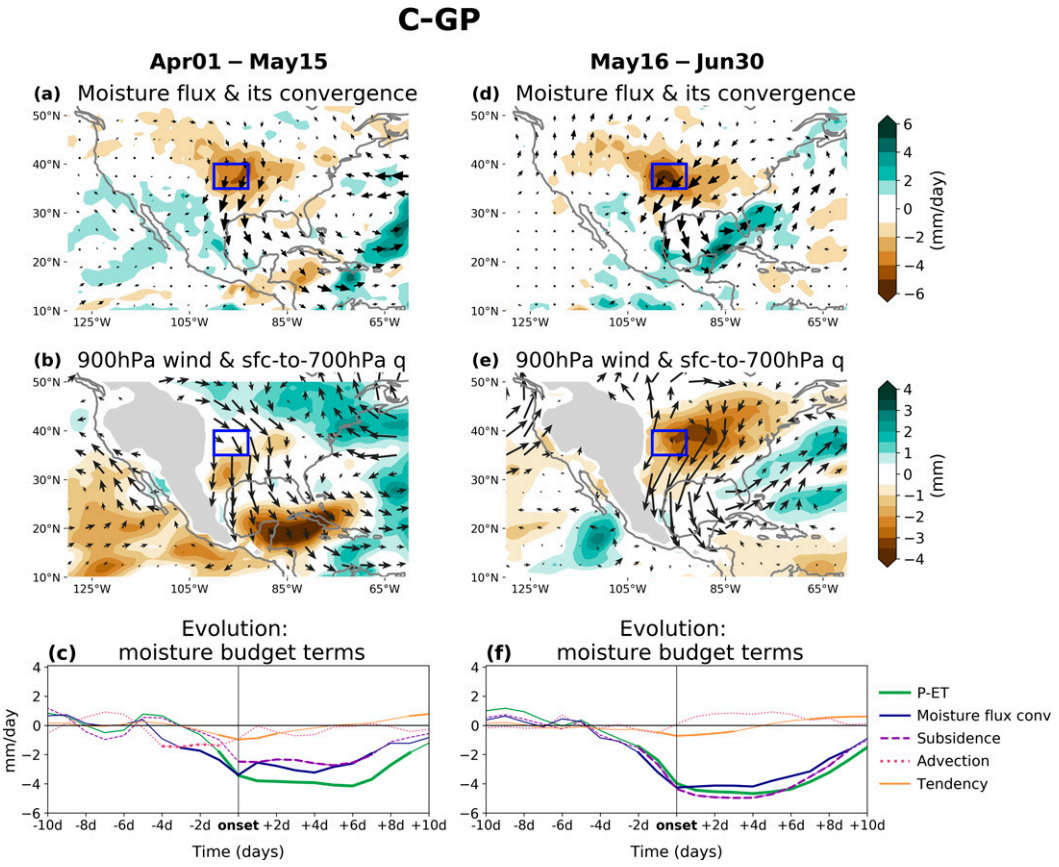


FIG. 10. Composites of (a),(d) anomalous column-integrated moisture flux (arrows) and its convergence (shading; mm day$^{-1}$) and (b),(e) 900-hPa horizontal wind anomalies (arrows) and anomalous low-level moisture (shading; mm) for the C-GP persistent $P-$ET deficit events in (a),(b) early and (d),(e) late spring at the onset. In (b) and (e), low-level moisture is specific humidity integrating from surface pressure level to 700 hPa. Regions where surface pressure levels are above 900 hPa are masked out. The region of the C-GP is indicated by the blue boxes. (c),(f) The composite evolution of each term in Eqs. (1) and (3), averaged over the C-GP. Solid lines represent each term in the atmospheric moisture budget [Eq. (1)]: green lines are the anomalous $P-$ET, navy lines are the anomalous convergence of column-integrated moisture flux, and orange lines are the tendency term. The two components of the convergence of column-integrated moisture flux [Eq. (3)] are shown in purple dashed lines (subsidence term) and pink dotted lines (advection term). The thicker lines denote the anomalies that significantly differ from zero.

to large-scale RWPs. These regions consequently became moisture sources for other remote regions (Figs. 7 and 10). Basic conservation arguments suggest that this moisture must come from the land surface, eventually leading to a soil moisture deficit there as well. Thus, we additionally examined the evolution of soil moisture corresponding to the composite evolution described above. Only the results for the Ohio Valley are shown here (Fig. 12); results for the C-GP and N-GP regions are qualitatively similar (Figs. S4 and S5).

The composite evolution of $P-$ET anomalies (Fig. 12, top row) shows that the persistent $P-$ET deficits are not systematically preceded by other persistent $P-$ET deficits, although some examples are found. Correspondingly, antecedent composite soil moisture is near average (Fig. 12, second row), albeit with substantial event-to-event differences. At event onset, composite soil moisture rapidly decreases in response to the developing $P-$ET deficits, declining from the 50th to below the 20th percentile within about five days. This rapid decline is seen in both the JRA-55 (brown lines) and CLM (orange lines) soil moisture products. Note that the pronounced steep decline in soil moisture percentile after event onset occurs for the individual events as well, despite their different antecedent soil moisture conditions (gray lines in Fig. 12, second row).

As noted earlier, warm temperature anomalies emerge *after* the initiation of soil moisture decline in both early and late spring (Fig. 12, third row). In fact, the temperature anomalies cool at event onset, consistent with strong anomalous diabatic cooling over the region (dark green lines in Fig. 12, bottom row) that is mainly due to evaporative cooling (light green lines). This supports the idea that as subsidence dries the atmospheric column, moisture is supplied from the land surface, leading to enhanced evaporation and hence near-surface cooling. While both adiabatic warming driven by subsidence

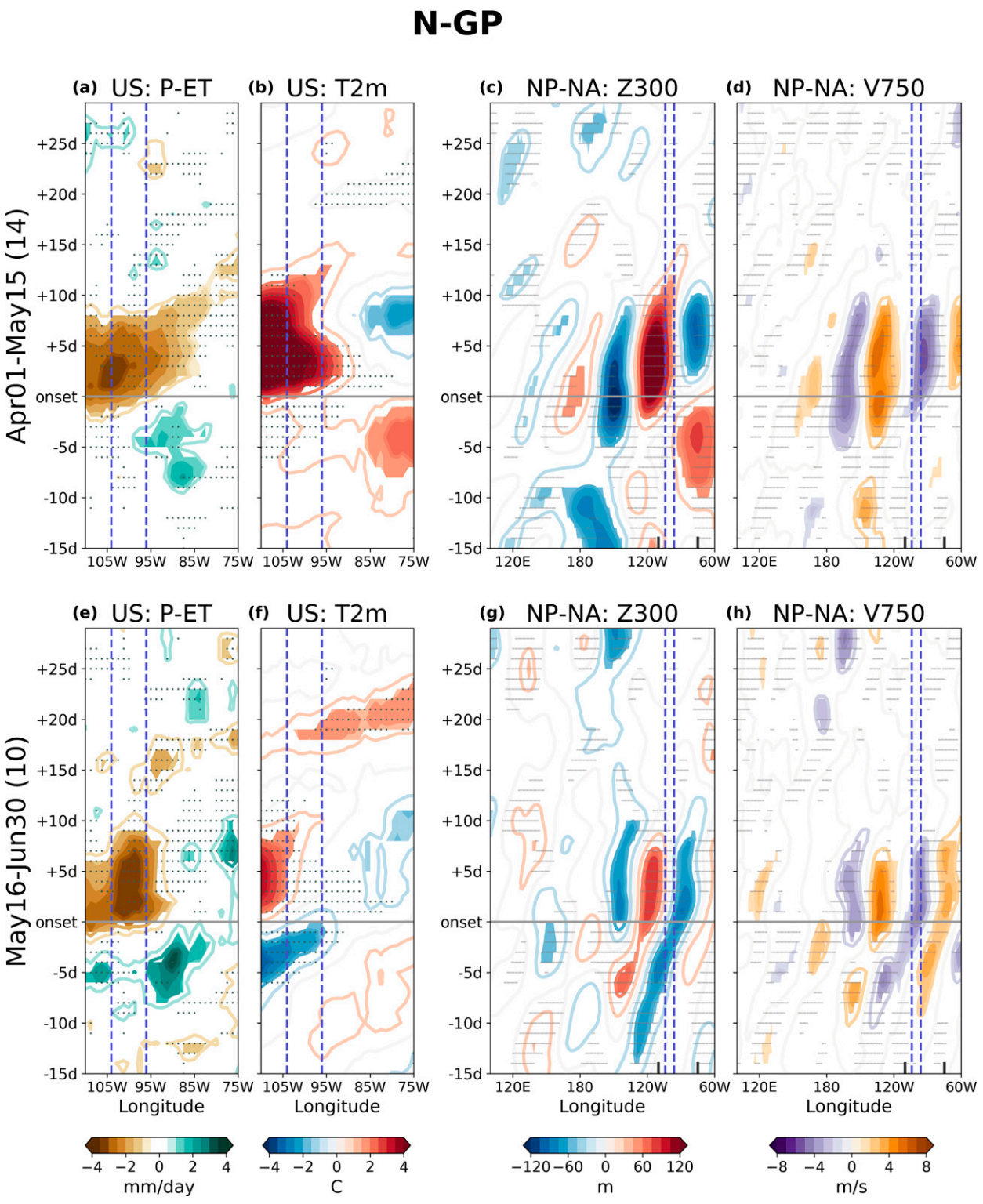


FIG. 11. Hovmöller diagrams for the composite persistent $P-$ ET deficit events for the N-GP region. (a),(e) $P-$ ET (mm day$^{-1}$) and (b),(f) T2m (°C) over the United States and (c),(g) Z300 (m) and (d),(h) V750 (m s$^{-1}$) anomalies across the NP-NA region in (top) early and (bottom) late spring. For $P-$ ET and T2m, the anomalies are averaged over 43°–48.5°N (see the N-GP box in Fig. 1). The anomalies of Z300 and V750 are averaged over 35°–55°N. Purple dashed lines indicate the longitudinal range of the N-GP area defined in Fig. 1 and Table 2. The longitudinal range for the United States in the left two columns is also labeled in the right two columns (black ticks). The statistically significant anomalies are shaded. Dots represent that the differences between early and late spring are statistically significant.

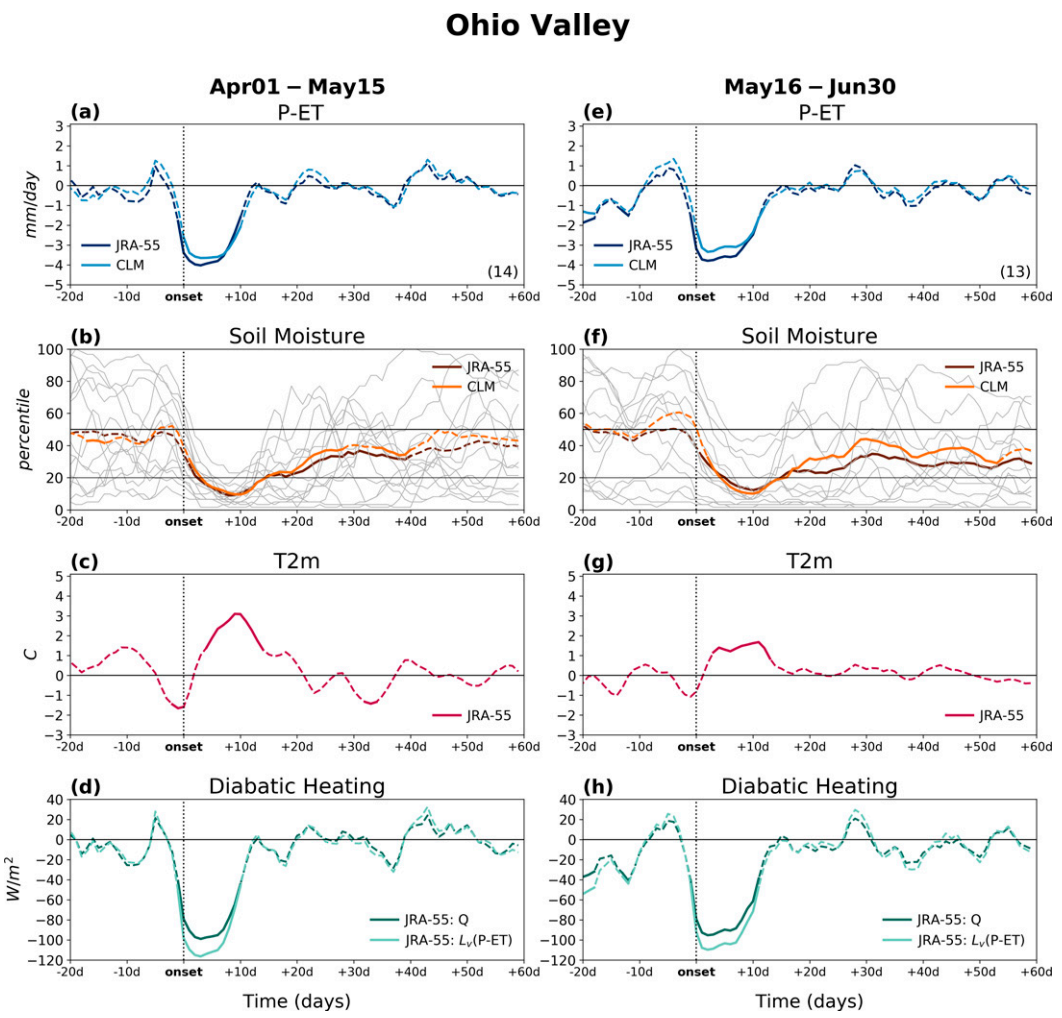


FIG. 12. Evolution of the composite persistent $P-$ ET deficit events averaged over the Ohio Valley region (see the Ohio Valley box in Fig. 1). (a),(e) $P-$ ET anomalies (mm day$^{-1}$), (b),(f) soil moisture (percentile), (c),(g) JRA-55 T2m anomalies (°C), and (d),(h) JRA-55 column-integrated diabatic heating anomalies (W m$^{-2}$) in (left) early and (right) late spring, from 20 days before the onset to 60 days after the onset. For $P-$ ET and soil moisture, data from JRA-55 (dark color) and CLM (light color) are both shown for comparison. The variations in soil moisture for individual events are indicated in gray thin lines in (b) and (f). For (d) and (h), column-integrated diabatic heating anomalies are shown in dark green lines, compared with calculated latent heating $L_v(P-\text{ET})$ (light green lines) where $L_v$ is the latent heat of vaporization. The solid lines denote the statistically significant anomalies.

and diabatic warming from increased incoming solar radiation may also occur, they appear insufficient to initially overcome the evaporative cooling. Eventually, with drying surface conditions, warming does overcome cooling and surface temperatures increase, after event onset. The evolution of these variables suggests that anomalous surface warmth is unlikely to play a critical role in triggering the rapid decline in soil moisture, in any of these three regions in either early or late spring.

While soil moisture declines rapidly in response to the persistent atmospheric moisture deficit, it recovers much more gradually, leading to prolonged anomalous root-zone dryness well after the $P-$ ET anomaly has returned to normal. In early spring (Fig. 12b), it takes about a month after the onset for the composite soil moisture deficits to rise above the 30th percentile level. In late spring (Fig. 12f), however, soil moisture dryness persists more than two months on average. These results, as well as those of the other two regions, suggest that extended periods of low soil moisture levels may be initiated by extreme atmospheric anomalies persisting only a little over a week.

The composite relationship between persistent $P-$ ET deficits, rapid decline in soil moisture, and lagged near-surface warmth captures details observed in some past springtime subseasonal drought events. For example, in late May 1980, large-scale circulation anomalies extending from the North

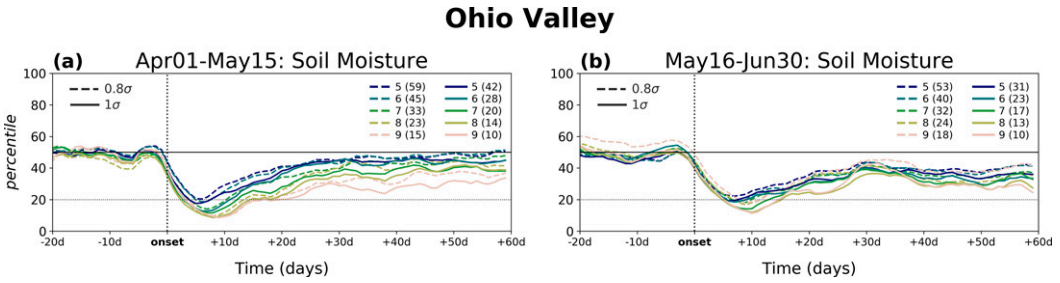


FIG. 13. Temporal evolution of the JRA-55 soil moisture composite for the Ohio Valley region based on different criteria for persistent $P-$ ET deficits in (a) early and (b) late spring, from 20 days before the onset to 60 days after the onset. Solid (dashed) lines are based on $-1$ ($-0.8$) standard deviation as the threshold for intensity. Different colors of line indicate different durations, from at least 5 days (navy) to at least 9 days (pink). The numbers of events based on each criterion are indicated in parentheses in the legends.

Pacific led to persistent precipitation deficits over the C-GP (Namias 1982; Lyon and Dole 1995). Soil moisture rapidly declined following the onset of the precipitation deficits (Mo and Lettenmaier 2016). Persistent record-breaking warm temperature anomalies did not show up until mid-June, well after the drought onset. Both soil moisture deficits and warm temperature anomalies persisted throughout the summer (Lyon and Dole 1995; Mo and Lettenmaier 2016). Similarly, for the 2017 northern Great Plains flash drought, precipitation deficits persisted from late April to early May, triggering soil moisture declines from above the 80th percentile to below the 20th percentile in one month (Hoell et al. 2019b; Pendergrass et al. 2020). Temperature anomalies were persistently negative in late April and did not become persistently warm until early May, after the initiation of soil moisture decline. Soil moisture did not recover to normal conditions until mid-September (Hoell et al. 2019b; Chen et al. 2020; Pendergrass et al. 2020).

Finally, we tested the sensitivity of the development of the soil moisture deficits to different thresholds of intensity and duration used to define the $P-$ ET deficit events. Figure 13 shows that the rapid and large decline in soil moisture following the $P-$ ET deficit onset is a robust feature of the event composites, especially during late spring. In response to varying the intensity and duration thresholds used to determine the $P-$ ET deficit composites, the primary difference in the soil moisture response is the duration of the resulting drought. In general, the initial decrease of soil moisture is about 30 percentiles in less than two weeks, in both early and late spring.

## 6. Concluding remarks

In this study, we developed a more comprehensive picture of the role of persistent atmospheric anomalies in initiating subseasonal drought development over the central United States during spring. The composite evolutions of persistent $P-$ ET deficits lasting at least one week over three central U.S. regions are related to quasi-stationary RWPs that extend from the western North Pacific to North America. The RWPs impose an anomalous ridge to the west of each region, inducing strong downstream subsidence and the resulting low-level divergent outflow, which dries the atmosphere and drives moisture out of the region, leading to persistent $P-$ ET deficits. The land supplies its available moisture to the atmosphere and the resulting soil moisture deficits could persist one month or longer, especially in late spring. Anomalous surface warmth does not develop until after the drought onset and is preceded by anomalous diabatic cooling at the onset.

We conclude that, during spring in the central United States, rapid decline in anomalous soil moisture is driven *dynamically* by atmospheric drying due to large-scale subsidence and the resulting low-level divergent outflow, rather than *thermodynamically* by drying due to anomalously warm near-surface temperatures. In our observational analysis, strong and persistent $P-$ ET deficits initially correspond to strong subsidence (Figs. 6 and 7), which also corresponds to diabatic cooling (Figs. 5 and 12) that is a consequence of strong anomalous evaporation. This suggests that, in an energy-limited area such as the springtime central United States, the subsidence dynamically enhances the atmospheric demand for moisture (also called evaporative demand; e.g., Hobbins et al. 2016), wherein the atmosphere draws moisture from the land surface, leading to enhanced evaporation and hence anomalous surface cooling (Fig. 12). Without replenishment from precipitation, the soil moisture eventually cannot meet the evaporative demand, leading to a decrease in latent heat flux. Then, in the face of continued subsidence and related adiabatic warming, an increase in sensible heat flux and the attendant surface warmth must emerge (e.g., Seneviratne et al. 2010; Berg et al. 2014), after the drought onset, to maintain the surface energy balance. That is, the subsidence exerted by the large-scale RWP dynamically dries the land surface, inducing the drought, and then warms the surface: surface warmth is a consequence rather than a cause of the drought.

In our composites, the rapid decline in soil moisture behaves like flash drought (e.g., Hunt et al. 2009; Otkin et al. 2016). In fact, one current flash drought definition is based upon the criterion that soil moisture has declined from above the 40th percentile to below the 20th percentile over a period shorter than 20 days (e.g., Ford and Labosier 2017; Koster et al. 2019; Lisonbee et al. 2021), consistent with the decline

rate of soil moisture in our composites (Fig. 12, second row). The rapid onset of flash drought has been attributed to an initial increase in evaporative demand due to high surface temperature (e.g., Otkin et al. 2013, 2018; Ford and Labosier 2017) and the resulting land–atmosphere coupling that accelerates the depletion in soil moisture. Thus, many other flash drought definitions have focused on evaporative demand–related indices, including the evaporative demand drought index (EDDI; e.g., Hobbins et al. 2016; Pendergrass et al. 2020; Lisonbee et al. 2021), rapid change in the evaporative stress index (RCI; e.g., Otkin et al. 2014; Chen et al. 2020; Lisonbee et al. 2021), and standard evaporative stress ratio (SESR; e.g., Christian et al. 2019; Lisonbee et al. 2021). It would be interesting to examine whether in our composites, the change in evaporative demand is consistent with these flash drought definitions.

Our composites, however, were based upon persistent deficits in atmospheric moisture supply, or $P - \mathrm{ET}$, without tailoring our definition to some of those common characteristics emphasized in previous flash drought studies. Also, we selected our events based on intensity and duration of the $P - \mathrm{ET}$ deficits, without considering the rapidity of the development. Nevertheless, in our $P - \mathrm{ET}$ composite events, the soil moisture deficits still rapidly developed, with warm temperature anomalies emerging *after* the initiation of soil moisture decline. This suggests that elevated temperature is not a necessary condition to trigger rapid soil moisture decline in spring. Of course, our composite analysis provides only an average across multiple events; some individual events preceded by large positive soil moisture anomalies could undergo considerable drying without reaching soil moisture drought conditions. The important conclusion that may be drawn from our results is that flash droughts can be induced by *dynamically driven* enhanced evaporative demand leading to persistent $P - \mathrm{ET}$ deficits.

Some previous studies indicated that subseasonal persistent dry episodes in the warm season in the central United States are likely influenced by suppressing northward moisture transport of the Great Plains low-level jet (GPLLJ) (e.g., Mo et al. 1997; Schubert et al. 1998; Wang et al. 2019). The warm season subseasonal drought could also be attributed to dry advection (Schiraldi and Roundy 2017). In contrast, our results suggested that local subsidence and the resulting low-level divergent outflow associated with the RWPs, rather than advection of anomalously drier air, are primarily responsible for the springtime subseasonal drought development. One possible explanation for this discrepancy is that previous studies included spring and summer together, whereas we have focused only on spring. On the other hand, note that low-level northerly wind anomalies are generally present in our composites, but their impact within the moisture budget, and therefore on the $P - \mathrm{ET}$ deficit, appears to be mostly secondary. A detailed moisture budget analysis, using different time scales for spring and summer separately, may be more suitable for understanding regarding the relationship between central U.S. precipitation variability and large-scale circulations including the GPLLJ.

We separated early and late spring due to the climatological change in the North Pacific Rossby waveguide in mid-May. Our results suggested that the separation was necessary even though we reduced the sample size by doing so. The horizontal scales of the RWPs significantly decrease from early to late spring. Also, the late spring RWPs display a faster group velocity but slower phase propagation, compared to early spring. As a result, the downstream persistent atmospheric forcing exerted by the RWPs may be more localized in late spring. The similarity and dissimilarity of hydroclimatic variability between regions within the central United States may also change from early to late spring. For example, the C-GP and N-GP are often influenced by the same wave train in early spring, but not in late spring. All these early–late spring differences suggest that in studying the warm season hydroclimatic variability in the central United States, treating the spring season or warm season as a whole would introduce misleading signal or causality through averaging two different phenomena with distinct backgrounds (e.g., Namias 1983; Newman and Sardeshmukh 1998).

Our composites captured recurring features seen in many historical springtime subseasonal droughts. However, whether there is any systematic remote forcing linked to these wave trains is less clear. This could be due to large event-to-event differences in the remote atmospheric forcing sources among the historical events. Alternatively, these quasi-stationary RWPs might be triggered by localized short-lived tropical heating events, rather than steady tropical forcing that our composites would highlight. Branstator (2014), using atmospheric general circulation model experiments, showed that a pulse of tropical forcing persisting for only two days could trigger a quasi-stationary Rossby wave propagating across the extratropical NP-NA sector and remaining for over two weeks. Such forcing sources, especially if they are relatively small scale, might be difficult to clearly identify and diagnose in our composite analysis. Future work could disentangle the potential source of the RWPs, including using idealized model experiments forced with regional diabatic heating anomalies to diagnose how the change in the basic state from early to late spring changes the resulting large-scale wave trains. Such experiments could also evaluate how the strong diabatic cooling within the drought region might feed back on the atmospheric anomaly there, and lead to further understanding of the predictability of springtime large-scale circulation anomalies and hence the downstream drought development, which may change during the spring season.

Our analysis for the central United States suggests that rapidly developing springtime droughts are typically dynamically driven by persistent atmospheric forcing related to large-scale wave trains crossing the North Pacific. Hence, related springtime soil moisture deficits appear "demand driven," with the atmosphere continuously drawing moisture from the climatologically moist underlying land surface, rather than "supply driven" due to the reduced moisture transport, say from the GPLLJ. These deficits then can persist for a month or more, suggesting that even though the atmospheric forcing and the resulting rapid drought onset may only be predictable over a week or two, an upcoming subseasonal agricultural drought

may be predictable once the upstream RWP forcing has begun.

*Acknowledgments.* Bor-Ting Jong was funded by the NOAA Physical Sciences Laboratory through National Research Council (NRC) Research Associateship Programs. The authors gratefully acknowledge support from the National Integrated Drought Information System. The JRA-55 reanalysis daily data were derived from the Research Data Archive at National Center for Atmospheric Research (NCAR). We thank Dr. Michael Hobbins, Dr. Min-Hui Lo, and three anonymous reviewers for their constructive comments.

## REFERENCES

AghaKouchak, A., 2014: A baseline probabilistic drought forecasting framework using standardized soil moisture index: Application to the 2012 United States drought. *Hydrol. Earth Syst. Sci.*, **18**, 2485–2492, https://doi.org/10.5194/hess-18-2485-2014.

Agrawal, S., C. R. Ferguson, L. Bosart, and D. A. Burrows, 2021: Teleconnections governing the interannual variability of Great Plains low-level jets in May. *J. Climate*, **34**, 4785–4806, https://doi.org/10.1175/JCLI-D-20-0451.1.

Anderson, W., R. Seager, W. Baethgen, and M. Cane, 2017: Life cycles of agriculturally relevant ENSO teleconnections in North and South America. *Int. J. Climatol.*, **37**, 3297–3318, https://doi.org/10.1002/joc.4916.

Atlas, R., N. Wolfson, and J. Terry, 1993: The effect of SST and soil moisture anomalies on GLA model simulations of the 1988 U.S. summer drought. *J. Climate*, **6**, 2034–2048, https://doi.org/10.1175/1520-0442(1993)006<2034:TEOSAS>2.0.CO;2.

Basara, J. B., J. I. Christian, R. A. Wakefield, J. A. Otkin, E. H. Hunt, and D. P. Brown, 2019: The evolution, propagation, and spread of flash drought in the Central United States during 2012. *Environ. Res. Lett.*, **14**, 084025, https://doi.org/10.1088/1748-9326/ab2cc0.

Berg, A., B. R. Lintner, K. L. Findell, S. Malyshev, P. C. Loikith, and P. Gentine, 2014: Impact of soil moisture–atmosphere interactions on surface temperature distribution. *J. Climate*, **27**, 7976–7993, https://doi.org/10.1175/JCLI-D-13-00591.1.

Branstator, G., 2014: Long-lived response of the midlatitude circulation and storm tracks to pulses of tropical heating. *J. Climate*, **27**, 8809–8826, https://doi.org/10.1175/JCLI-D-14-00312.1.

Breeden, M. L., A. H. Butler, J. R. Albers, M. Sprenger, and A. O. Langford, 2021: The spring transition of the North Pacific jet and its relation to deep stratosphere-to-troposphere mass transport over western North America. *Atmos. Chem. Phys.*, **21**, 2781–2794, https://doi.org/10.5194/acp-21-2781-2021.

Chang, F.-C., and J. M. Wallace, 1987: Meteorological conditions during heat waves and droughts in the United States Great Plains. *Mon. Wea. Rev.*, **115**, 1253–1269, https://doi.org/10.1175/1520-0493(1987)115<1253:MCDHWA>2.0.CO;2.

Chen, L. G., A. Hartman, B. Pugh, J. Gottschalck, and D. Miskus, 2020: Real-time prediction of areas susceptible to flash drought development. *Atmosphere*, **11**, 1114, https://doi.org/10.3390/atmos11101114.

Chen, P., and M. Newman, 1998: Rossby wave propagation and the rapid development of upper-level anomalous anticyclones during the 1988 U.S. drought. *J. Climate*, **11**, 2491–2504, https://doi.org/10.1175/1520-0442(1998)011<2491:RWPATR>2.0.CO;2.

Christian, J. I., J. B. Basara, J. A. Otkin, E. D. Hunt, R. A. Wakefield, P. X. Flanagan, and X. Xiao, 2019: A methodology for flash drought identification: Application of flash drought frequency across the United States. *J. Hydrometeor.*, **20**, 833–846, https://doi.org/10.1175/JHM-D-18-0198.1.

Cook, B. I., R. Seager, and R. L. Miller, 2011: Atmospheric circulation anomalies during two persistent North American droughts: 1932–1939 and 1948–1957. *Climate Dyn.*, **36**, 2339–2355, https://doi.org/10.1007/s00382-010-0807-1.

DeAngelis, A. M., H. Wang, R. D. Koster, S. D. Schubert, Y. Chang, and J. Marshak, 2020: Prediction skill of the 2012 U.S. Great Plains flash drought in subseasonal experiment (SubX) models. *J. Climate*, **33**, 6229–6253, https://doi.org/10.1175/JCLI-D-19-0863.1.

Diaz, H. F., 1983: Drought in the United States: Some aspects of major dry and wet periods in the contiguous United States, 1895–1981. *J. Appl. Meteor. Climatol.*, **22**, 3–16, https://doi.org/10.1175/1520-0450(1983)022<0003:DITUS>2.0.CO;2.

Dole, R., and N. D. Gordon, 1983: Persistent anomalies of the extratropical Northern Hemisphere wintertime circulation: Geographical distribution and regional persistent characteristics. *Mon. Wea. Rev.*, **111**, 1567–1586, https://doi.org/10.1175/1520-0493(1983)111<1567:PAOTEN>2.0.CO;2.

Dong, X., and Coauthors, 2011: Investigation of the 2006 drought and 2007 flood extremes at the southern Great Plains through an integrative analysis of observations. *J. Geophys. Res.*, **116**, D03204, https://doi.org/10.1029/2010JD014776.

Englehart, P. J., and A. V. Douglas, 2003: Assessing warm season drought episodes in the central United States. *J. Climate*, **16**, 1831–1842, https://doi.org/10.1175/1520-0442(2003)016<1831:AWSDEI>2.0.CO;2.

Erfanian, A., and R. Fu, 2019: The role of spring dry zonal advection in summer drought onset over the US Great Plains. *Atmos. Chem. Phys.*, **19**, 15 199–15 216, https://doi.org/10.5194/acp-19-15199-2019.

Fernando, D. N., and Coauthors, 2016: What caused the spring intensification and winter demise of the 2011 drought over Texas? *Climate Dyn.*, **47**, 3077–3090, https://doi.org/10.1007/s00382-016-3014-x.

Ford, T. W., and C. F. Labosier, 2017: Meteorological conditions associated with the onset of flash drought in the eastern United States. *Agric. For. Meteor.*, **247**, 414–423, https://doi.org/10.1016/j.agrformet.2017.08.031.

Gerken, T., G. T. Bromley, B. L. Ruddell, S. Williams, and P. C. Stoy, 2018: Convective suppression before and during the United States northern Great Plains flash drought of 2017. *Hydrol. Earth Syst. Sci.*, **22**, 4155–4163, https://doi.org/10.5194/hess-22-4155-2018.

Ghannam, K., T. Nakai, A. Paschalis, C. A. Oishi, A. Kotani, Y. Igarashi, T. Kumagai, and G. G. Katul, 2016: Persistence and memory timescales in root-zone soil moisture dynamics. *Water Resour. Res.*, **52**, 1427–1445, https://doi.org/10.1002/2015WR017983.

Hansen, N. C., B. L. Allen, R. L. Baumhardt, and D. J. Lyon, 2012: Research achievements and adoption of no-till, dryland cropping in the semi-arid U.S. Great Plains. *Field Crops Res.*, **132**, 196–203, https://doi.org/10.1016/j.fcr.2012.02.021.

Hao, Z., V. P. Singh, and Y. Xia, 2018: Seasonal drought prediction: Advances, challenges, and future prospects. *Rev. Geophys.*, **56**, 108–141, https://doi.org/10.1002/2016RG000549.

Harding, K. J., and P. K. Snyder, 2015: The relationship between the Pacific–North American teleconnection pattern, the Great Plains low-level jet, and north central U.S. heavy rainfall events. *J. Climate*, **28**, 6729–6742, https://doi.org/10.1175/JCLI-D-14-00657.1.

Hobbins, M. T., A. Wood, D. J. Mcevoy, J. L. Huntington, C. Morton, M. Anderson, and C. Hain, 2016: The Evaporative Demand Drought Index. Part I: Linking drought evolution to variations in evaporative demand. *J. Hydrometeor.*, **17**, 1745–1761, https://doi.org/10.1175/JHM-D-15-0121.1.

Hoell, A., J. Perlwitz, C. Dewes, K. Wolter, I. Rangwala, X.-W. Quan, and J. Eischeid, 2019a: Anthropogenic contributions to the intensity of the 2017 United States northern Great Plains drought (in "Explaining Extreme Events of 2017 from a Climate Perspective"). *Bull. Amer. Meteor. Soc.*, **100**(1), S19–S24, https://doi.org/10.1175/BAMS-D-18-0127.1.

——, ——, and J. Eischeid, 2019b: Drought assessment report: The causes, predictability, and historical context of the 2017 U.S. northern Great Plains drought. National Integrated Drought Information System Rep., 27 pp., https://www.drought.gov/sites/default/files/2020-09/2017-NGP-drought-assessment.pdf.

——, and Coauthors, 2020: Lessons learned from the 2017 flash drought across the U.S. northern Great Plains and Canadian prairies. *Bull. Amer. Meteor. Soc.*, **101**, E2171–E2185, https://doi.org/10.1175/BAMS-D-19-0272.1.

Hoerling, M. P., and Coauthors, 2013: Anatomy of an extreme event. *J. Climate*, **26**, 2811–2832, https://doi.org/10.1175/JCLI-D-12-00270.1.

——, J. Eischeid, A. Kumar, A. Mariotti, K. C. Mo, S. D. Schubert, and R. Seager, 2014: Causes and predictability of the 2012 Great Plains drought. *Bull. Amer. Meteor. Soc.*, **95**, 269–282, https://doi.org/10.1175/BAMS-D-13-00055.1.

Hong, S.-Y., and E. Kalnay, 2000: Role of sea surface temperature and soil-moisture feedback in the 1998 Oklahoma–Texas drought. *Nature*, **408**, 842–844, https://doi.org/10.1038/35048548.

Hoskins, B. J., and T. Ambrizzi, 1993: Rossby wave propagation on a realistic longitudinally varying flow. *J. Atmos. Sci.*, **50**, 1661–1671, https://doi.org/10.1175/1520-0469(1993)050<1661:RWPOAR>2.0.CO;2.

——, and K. I. Hodges, 2019: The annual cycle of Northern Hemisphere storm tracks. Part II: Regional detail. *J. Climate*, **32**, 1761–1775, https://doi.org/10.1175/JCLI-D-17-0871.1.

Hu, Q. I., and G. Buyanovsky, 2003: Climate effects on corn yield in Missouri. *J. Appl. Meteor. Climatol.*, **42**, 1626–1635, https://doi.org/10.1175/1520-0450(2003)042<1626:CEOCYI>2.0.CO;2.

Huang, C., S. W. Duiker, L. Deng, C. Fang, and W. Zeng, 2015: Influence of precipitation on maize yield in the eastern United States. *Sustainability*, **7**, 5996–6010, https://doi.org/10.3390/su7055996.

Hunt, E. D., K. G. Hubbard, D. A. Wilhite, T. J. Arkebauer, and A. L. Dutcher, 2009: The development and evaluation of a soil moisture index. *Int. J. Climatol.*, **29**, 747–759, https://doi.org/10.1002/joc.1749.

JMA, 2014: JRA-55 product users' handbook. Climate Prediction Division, Japan Meteorological Agency, 27 pp., https://rda.ucar.edu/datasets/ds628.0/docs/JRA-55.handbook_TL319_en.pdf.

Kam, J., J. Sheffield, X. Yuan, and E. F. Wood, 2014: Did a skillful prediction of sea surface temperatures help or hinder forecasting of the 2012 Midwestern US drought? *Environ. Res. Lett.*, **9**, 034005, https://doi.org/10.1088/1748-9326/9/3/034005.

Karl, T. R., and R. G. Quayle, 1981: The 1980 summer heat wave and drought in historical perspective. *Mon. Wea. Rev.*, **109**, 2055–2073, https://doi.org/10.1175/1520-0493(1981)109<2055:TSHWAD>2.0.CO;2.

Kobayashi, S., and Coauthors, 2015: The JRA-55 reanalysis: General specifications and basic characteristics. *J. Meteor. Soc. Japan*, **93**, 5–48, https://doi.org/10.2151/jmsj.2015-001.

Koster, R. D., S. D. Schubert, and M. J. Suarez, 2009: Analyzing the concurrence of meteorological droughts and warm periods, with implications for the determination of evaporative regime. *J. Climate*, **22**, 3331–3341, https://doi.org/10.1175/2008JCLI2718.1.

——, ——, H. Wang, S. P. Mahanama, and A. M. DeAngelis, 2019: Flash drought as captured by reanalysis data: Disentangling the contributions of precipitation deficit and excess evapotranspiration. *J. Hydrometeor.*, **20**, 1241–1258, https://doi.org/10.1175/JHM-D-18-0242.1.

Kumar, A., M. Chen, M. Hoerling, and J. Eischeid, 2013: Do extreme climate events require extreme forcings? *Geophys. Res. Lett.*, **40**, 3440–3445, https://doi.org/10.1002/grl.50657.

Li, M., P. Wu, and Z. Ma, 2020: A comprehensive evaluation of soil moisture and soil temperature from third-generation atmospheric and land reanalysis data sets. *Int. J. Climatol.*, **40**, 5744–5766, https://doi.org/10.1002/joc.6549.

Lisonbee, J., M. Woloszyn, and M. Skumanich, 2021: Making sense of flash drought: Definitions, indicators, and where we go from here. *J. Appl. Serv. Climatol.*, **2021** (1), 1–19, https://doi.org/10.46275/JOASC.2021.02.001.

Liu, A. Z., M. Ting, and H. Wang, 1998: Maintenance of circulation anomalies during the 1988 drought and 1993 floods over the United States. *J. Atmos. Sci.*, **55**, 2810–2832, https://doi.org/10.1175/1520-0469(1998)055<2810:MOCADT>2.0.CO;2.

Livneh, B., and M. P. Hoerling, 2016: The physics of drought in the U.S. central Great Plains. *J. Climate*, **29**, 6783–6804, https://doi.org/10.1175/JCLI-D-15-0697.1.

Lyon, B., and R. Dole, 1995: A diagnostic comparison of the 1980 and 1988 U.S. summer heat wave–droughts. *J. Climate*, **8**, 1658–1675, https://doi.org/10.1175/1520-0442(1995)008<1658:ADCOTA>2.0.CO;2.

Miller, R. L., G. M. Lackmann, and W. A. Robinson, 2020: A new variable-threshold persistent anomaly index: Northern Hemisphere anomalies in the ERA-Interim reanalysis. *Mon. Wea. Rev.*, **148**, 43–62, https://doi.org/10.1175/MWR-D-19-0144.1.

Mo, K. C., 2011: Drought onset and recovery over the United States. *J. Geophys. Res.*, **116**, D20106, https://doi.org/10.1029/2011JD016168.

——, and D. P. Lettenmaier, 2015: Heat wave flash droughts in decline. *Geophys. Res. Lett.*, **42**, 2823–2829, https://doi.org/10.1002/2015GL064018.

——, and ——, 2016: Precipitation deficit flash droughts over the United States. *J. Hydrometeor.*, **17**, 1169–1184, https://doi.org/10.1175/JHM-D-15-0158.1.

——, J. R. Zimmerman, E. Kalnay, and M. Kanamitsu, 1991: A GCM study of the 1988 United States drought. *Mon. Wea. Rev.*, **119**, 1512–1532, https://doi.org/10.1175/1520-0493(1991)119<1512:AGSOTU>2.0.CO;2.

——, J. N. Paegle, and R. W. Higgins, 1997: Atmospheric processes associated with summer floods and droughts in the central United States. *J. Climate*, **10**, 3028–3046, https://doi.org/10.1175/1520-0442(1997)010<3028:APAWSF>2.0.CO;2.

Namias, J., 1982: Anatomy of Great Plains protracted heat waves (especially the 1980 U.S. summer drought). *Mon. Wea. Rev.*,

**110**, 824–838, https://doi.org/10.1175/1520-0493(1982)110<0824:AOGPPH>2.0.CO;2.

——, 1983: Some causes of United States drought. *J. Appl. Meteor. Climatol.*, **22**, 30–39, https://doi.org/10.1175/1520-0450(1983)022<0030:SCOUSD>2.0.CO;2.

——, 1991: Spring and summer 1988 drought over the contiguous United States—Causes and prediction. *J. Climate*, **4**, 54–65, https://doi.org/10.1175/1520-0442(1991)004<0054:SASDOT>2.0.CO;2.

Newman, M., and P. D. Sardeshmukh, 1998: The impact of the annual cycle on the North Pacific/North American response to remote low-frequency forcing. *J. Atmos. Sci.*, **55**, 1336–1353, https://doi.org/10.1175/1520-0469(1998)055<1336:TIOTAC>2.0.CO;2.

——, G. N. Kiladis, K. M. Weickmann, M. F. Ralph, and P. D. Sardeshmukh, 2012: Relative contributions of synoptic and low-frequency eddies to time-mean atmospheric moisture transport, including the role of atmospheric rivers. *J. Climate*, **25**, 7341–7361, https://doi.org/10.1175/JCLI-D-11-00665.1.

NIDIS, 2021: Drought basics: Types of drought. National Integrated Drought Information System, accessed 2021, https://www.drought.gov/what-is-drought/drought-basics#types-of-drought.

Oleson, K., and Coauthors, 2013: Technical description of version 4.5 of the Community Land Model (CLM). NCAR Tech. Note NCAR/TN-503+STR, 420 pp., https://doi.org/10.5065/D6RR1W7M.

Otkin, J. A., M. C. Anderson, C. Hain, I. E. Mladenova, J. B. Basara, and M. Svoboda, 2013: Examining rapid onset drought development using the thermal infrared-based evaporative stress index. *J. Hydrometeor.*, **14**, 1057–1074, https://doi.org/10.1175/JHM-D-12-0144.1.

——, ——, ——, and M. Svoboda, 2014: Examining the relationship between drought development and rapid changes in the evaporative stress index. *J. Hydrometeor.*, **15**, 938–956, https://doi.org/10.1175/JHM-D-13-0110.1.

——, and Coauthors, 2016: Assessing the evolution of soil moisture and vegetation conditions during the 2012 United States flash drought. *Agric. For. Meteor.*, **218–219**, 230–242, https://doi.org/10.1016/j.agrformet.2015.12.065.

——, M. Svoboda, E. D. Hunt, T. W. Ford, M. C. Anderson, C. Hain, and J. B. Basara, 2018: Flash droughts: A review and assessment of the challenges imposed by rapid-onset droughts in the United States. *Bull. Amer. Meteor. Soc.*, **99**, 911–919, https://doi.org/10.1175/BAMS-D-17-0149.1.

PaiMazumder, D., and J. M. Done, 2016: Potential predictability sources of the 2012 U.S. drought in observations and a regional model ensemble. *J. Geophys. Res. Atmos.*, **121**, 12 581–12 592, https://doi.org/10.1002/2016JD025322.

Palmer, T. N., and Č. Branković, 1989: The 1988 US drought linked to anomalous sea surface temperature. *Nature*, **338**, 54–57, https://doi.org/10.1038/338054a0.

Peixoto, J. P., and A. H. Oort, 1992: *Physics of Climate*. American Institute of Physics, 520 pp.

Pendergrass, A. G., and Coauthors, 2020: Flash droughts present a new challenge for subseasonal-to-seasonal prediction. *Nat. Climate Change*, **10**, 191–199, https://doi.org/10.1038/s41558-020-0709-0.

Quan, X.-W., M. P. Hoerling, B. Lyon, A. Kumar, M. A. Bell, M. K. Tippett, and H. Wang, 2012: Prospects for dynamical prediction of meteorological drought. *J. Appl. Meteor. Climatol.*, **51**, 1238–1252, https://doi.org/10.1175/JAMC-D-11-0194.1.

Roy, T., J. A. Martinez, J. E. Herrera-Estrada, Y. U. Zhang, F. Dominguez, A. Berg, M. Ek, and E. F. Wood, 2019: Role of moisture transport and recycling in characterizing droughts: Perspectives from two recent U.S. droughts and the CFSv2 system. *J. Hydrometeor.*, **20**, 139–154, https://doi.org/10.1175/JHM-D-18-0159.1.

Sato, N., P. J. Sellers, D. A. Randall, E. K. Schneider, J. Shukla, J. L. Kinter III, and E. Albertazzi, 1989: Effects of implementing the simple biosphere model in a general circulation model. *J. Atmos. Sci.*, **46**, 2757–2782, https://doi.org/10.1175/1520-0469(1989)046<2757:EOITSB>2.0.CO;2.

Scannell, H. A., A. J. Pershing, M. A. Alexander, A. C. Thomas, and K. E. Mills, 2016: Frequency of marine heatwaves in the North Atlantic and North Pacific since 1950. *Geophys. Res. Lett.*, **43**, 2069–2076, https://doi.org/10.1002/2015GL067308.

Schiraldi, N. J., and P. E. Roundy, 2017: The evolution of agricultural drought transition periods in the U.S. Corn Belt. *Mon. Wea. Rev.*, **145**, 451–472, https://doi.org/10.1175/MWR-D-16-0225.1.

Schubert, S. D., H. M. Helfand, C.-Y. Wu, and W. Min, 1998: Subseasonal variations in warm-season moisture transport and precipitation over the central and eastern United States. *J. Climate*, **11**, 2530–2555, https://doi.org/10.1175/1520-0442(1998)011<2530:SVIWSM>2.0.CO;2.

——, and Coauthors, 2016: Global meteorological drought: A synthesis of current understanding with a focus on SST drivers of precipitation deficits. *J. Climate*, **29**, 3989–4019, https://doi.org/10.1175/JCLI-D-15-0452.1.

Seager, R., and N. Henderson, 2013: Diagnostic computation of moisture budgets in the ERA-Interim reanalysis with reference to analysis of CMIP-archived atmospheric model data. *J. Climate*, **26**, 7876–7901, https://doi.org/10.1175/JCLI-D-13-00018.1.

——, and M. Hoerling, 2014: Atmosphere and ocean origins of North American droughts. *J. Climate*, **27**, 4581–4606, https://doi.org/10.1175/JCLI-D-13-00329.1.

——, L. Goddard, J. Nakamura, N. Henderson, and D. E. Lee, 2014: Dynamical causes of the 2010/11 Texas–northern Mexico drought. *J. Hydrometeor.*, **15**, 39–68, https://doi.org/10.1175/JHM-D-13-024.1.

——, J. Nakamura, and M. Ting, 2019: Mechanisms of seasonal soil moisture drought onset and termination in the southern Great Plains. *J. Hydrometeor.*, **20**, 751–771, https://doi.org/10.1175/JHM-D-18-0191.1.

——, ——, and ——, 2020: Prediction of seasonal meteorological drought onset and termination over the southern Great Plains in the North American Multimodel Ensemble. *J. Hydrometeor.*, **21**, 2237–2255, https://doi.org/10.1175/JHM-D-20-0023.1.

Sebastian, D. E., A. Pathak, and S. Ghosh, 2016: Use of atmospheric budget to reduce uncertainty in estimated water availability over South Asia from difference reanalyses. *Sci. Rep.*, **6**, 29664, https://doi.org/10.1038/srep29664.

Sellers, P. J., Y. Mintz, Y. C. Sud, and A. Dalcher, 1986: A Simple Biosphere model (SiB) for use within general circulation models. *J. Atmos. Sci.*, **43**, 505–531, https://doi.org/10.1175/1520-0469(1986)043<0505:ASBMFU>2.0.CO;2.

Seneviratne, S. I., T. Corti, E. L. Davin, M. Hirschi, E. B. Jaeger, I. Lehner, B. Orlowsky, and A. J. Teuling, 2010: Investigating soil moisture–climate interactions in a changing climate: A review. *Earth-Sci. Rev.*, **99**, 125–161, https://doi.org/10.1016/j.earscirev.2010.02.004.

Svoboda, M., and Coauthors, 2002: The Drought Monitor. *Bull. Amer. Meteor. Soc.*, **83**, 1181–1190, https://doi.org/10.1175/1520-0477-83.8.1181.

Trenberth, K. E., and G. W. Branstator, 1992: Issues in establishing causes of the 1988 drought over North America. *J. Climate*, **5**, 159–172, https://doi.org/10.1175/1520-0442(1992)005<0159:IIECOT>2.0.CO;2.

——, and C. Guillemot, 1996: Physical processes involved in the 1988 drought and 1993 floods in North America. *J. Climate*, **9**, 1288–1298, https://doi.org/10.1175/1520-0442(1996)009<1288:PPIITD>2.0.CO;2.

——, G. W. Branstator, and P. A. Arkin, 1988: Origins of the 1988 North American drought. *Science*, **242**, 1640–1645, https://doi.org/10.1126/science.242.4886.1640.

——, J. T. Fasullo, and J. Mackaro, 2011: Atmospheric moisture transports from ocean to land and global energy flows in reanalyses. *J. Climate*, **24**, 4907–4924, https://doi.org/10.1175/2011JCLI4171.1.

Van Loon, A. F., and Coauthors, 2016: Drought in the Anthropocene. *Nat. Geosci.*, **9**, 89–91, https://doi.org/10.1038/ngeo2646.

Viovy, N., and P. Ciais, 2011: CRUNCEP data set for 1901–2008. North American Carbon Program, Oak Ridge National Laboratory, accessed 2020, ftp://nacp.ornl.gov/synthesis/2009/frescati/temp/land_use_change/original/readme.htm.

Wang, H., S. D. Schubert, R. Koster, Y.-G. Ham, and M. Suarez, 2014: On the role of SST forcing in the 2011 and 2012 extreme U.S. heat and drought: A study in contrasts. *J. Hydrometeor.*, **15**, 1255–1273, https://doi.org/10.1175/JHM-D-13-069.1.

——, ——, and R. D. Koster, 2017: North American drought and links to northern Eurasia: The role of stationary Rossby waves. *Climate Extremes: Mechanisms and Potential Prediction*, S-.Y. S. Wang et al., Eds., Amer. Geophys. Union, 195–221.

——, ——, ——, and Y. Chang, 2019: Attribution of the 2017 northern high plains drought (in "Explaining Extreme Events of 2017 from a Climate Perspective"). *Bull. Amer. Meteor. Soc.*, **100** (1), S25–S29, https://doi.org/10.1175/BAMS-D-18-0115.1.

Wang, S. Y., and T. C. Chen, 2009: The late-spring maximum of rainfall over the U.S. central plains and the role of the low-level jet. *J. Climate*, **22**, 4696–4709, https://doi.org/10.1175/2009JCLI2719.1.

Weaver, S. J., and S. Nigam, 2008: Variability of the Great Plains low-level jet: Large-scale circulation context and hydroclimate impacts. *J. Climate*, **21**, 1532–1551, https://doi.org/10.1175/2007JCLI1586.1.

Wilhite, D. A., and M. H. Glantz, 1985: Understanding the drought phenomenon: The role of definitions. *Water Int.*, **10**, 111–120, https://doi.org/10.1080/02508068508686328.

Wirth, V., M. Riemer, E. K. M. Chang, and O. Martius, 2018: Rossby wave packets on the midlatitude waveguide—A review. *Mon. Wea. Rev.*, **146**, 1965–2001, https://doi.org/10.1175/MWR-D-16-0483.1.

Wolfson, N., R. Atlas, and Y. C. Sud, 1987: Numerical experiments related to the summer 1980 U.S. heat wave. *Mon. Wea. Rev.*, **115**(7), 1345–1357, https://doi.org/10.1175/1520-0493(1987)115<1345:NERTTS>2.0.CO;2.

Xu, T., M. Newman, A. Capotondi, and E. Di Lorenzo, 2021: The continuum of northeast Pacific marine heatwaves and their relationship to the tropical Pacific. *Geophys. Res. Lett.*, **48**, e2020GL090661, https://doi.org/10.1029/2020GL090661.

Zeng, X., 2001: Global vegetation root distribution for land modeling. *J. Hydrometeor.*, **2**, 525–530, https://doi.org/10.1175/1525-7541(2001)002<0525:GVRDFL>2.0.CO;2.